**OPERA Collaboration**


OPERA Internal note
July 06, 2001

# The scintillator option for the OPERA target tracker: results on the readout.

**L.Chaussard, P.Jonsson, S.Katsanevas, J.Marteau, G.Moret**
**S.Gardien, C.Girerd; D.Essertaize, G.Guillot, S.Vanzetto**

Institut de Physique Nucléaire de Lyon
Université Claude Bernard Lyon I
F-69622 Villeurbanne cedex

**Abstract**

This note summarizes the studies performed at the IPNL concerning the readout of the scintillator option of the target tracker (TT). In particular we review the performances and eventual limitations of the multipixel photodetector HPD, the autotriggerable low noise Viking Chips (VATA series) and an ethernet based DACQ system. We present beam tests, including the full readout chain from the photodetector to the workstation, with both the liquid and plastic scintillator options. Based on the above we present an alternative to the baseline option for the placement of the photodetectors. In this new architecture the photodetectors and the associated electronics are put at the corners of the walls, far from to the scintillator modules. We study the implications of this choice, and present work in progress concerning a prototype. We then review the implications of the current electronics for the readout and event-building architecture and present results on the simulation of the full DACQ structure.

# 1 Introduction

The baseline option of the OPERA target tracker foresees the use of plastic scintillator, read by a multi-pixel photo-detector (MaPMT) and auto-triggerable electronics. Tests and Monte-Carlo simulations have been undertaken in the collaboration, and in Lyon in particular, to characterize the performance of various alternatives [1].

In this note, in section 2 we present the tests we have performed with Hybrid Photo Diodes (HPD's), photodetectors that have recently reached a great level of maturity. We then proceed to present the characterization of the VATA autotriggerable electronics (section 3). These electronics are suitable, though different versions, for both the HPD and the MaPMT. The current performances are summarized and a set of benchmarks for the LAL/Strasbourg chip under construction are implicitly set. We then (section 4) present the data acquisition card ORCA, constructed in Lyon, and validated in beam tests, able to read the above front-end electronics and deliver the data directly to the Ethernet network. Section 5 presents the beam tests done with the full readout chain, with both plastic and liquid scintillator options. In section 6 we propose a target tracker architecture where the photodetectors are at the corners. In sections 7 and 8 we discuss the implications of the electronics for the triggering and event-building data-acquisition and we specify further our proposal for a fully Ethernet based DACQ. The first realistic finite-state machine simulations of a fully specified DACQ architecture are also shown. In the final section we recapitulate our findings and propositions on all items touched upon.

# 2 HPD characteristics

The HPD's are hybrid devices using a photocathode to convert photons into photo-electrons, accelerating the latter with a typical high voltage ranging from 8 to 10 kV. The 8-10 KeV photoelectrons impinging on a silicon sensor convert their energy to charge. The energy needed to create an electron-hole pair in silicon is $E_{e-h} = 3.62$ eV. The gain of the HPD is given by $G\,(e^-) \;=\; (U - U_0)\,(V) \;/\; E_{e-h}\,(eV)$, where $U$ is the applied high voltage and $U_0$ represents losses in the silicon dead-layer; the non-sensitive region. The typical gain of the HPD is 3000 corresponding to a charge of 0.5 fC.

Detailed studies have been performed in Lyon using a 61 pixels HPD model, produced by DEP [2], the characteristics of which are displayed in Table 1. Fig.1 shows the design of the 61 pixels HPD. Each pixel has its own feed-through and connecting pin[1].

The external dimensions of the HPD are 38 mm × 13 mm. The useful diameter of input window is 18 mm. The high voltage and ground connections use 2 wires on the side. The HPD tube is surrounded with a rubber coating for isolation. The input window lies $\sim 1$ mm under the surface of this coating. This is useful for the connection of the fiber cookie with the input window without imposing strong constraints on the tube itself.

The photo-cathode is deposited on a fiber optics entrance window. This gives very good performance for the HPD in terms of optical cross-talk (see Sect. 2.5). The photo-cathode is of multi-alkali S20 type. Its quantum efficiency as a function of the wavelength is detailed in Sect. 2.1 and Fig. 4.

In this proximity focused HPD the acceleration distance between photo-cathode and the silicon plane is a few millimeters. This makes the HPD immune to magnetic fields. The silicon sensor is divided in 61 hexagonal pixels. Each pixel is 2 mm side to side, with an active area of 3.5 mm$^2$. A depletion voltage of 60 V is required to fully deplete the silicon diode. The gap between 2 adjacent pixels is 50 $\mu$m and the electrical cross-talk is less than 1%. The output capacitance of the pixels is around 4 pF.

The front-end electronics of the HPD should have high gain and low noise. The low output capacitance allows the use of standard commercial chips originally designed for the readout of silicon detectors (see Sect. 3 for a complete description of the front-end electronics). We use VA-TA type electronic chips, directly bonded on a front-end board.

Many tests have been completed to characterize the HPD in terms of: resolution, uniformity, linearity, cross-talk, dark current with LED pulsed light and MIPS passing through the proposed scintillator detectors (plastic and liquid); we present them in the following.

[1] The pin-out is done through a standard 0.1" pin pitch PGA socket. This model has 80 pins, 61 for the signal, 2 for the ground connection, 4 for the bias of the PIN diode. Thirteen pins are not connected.

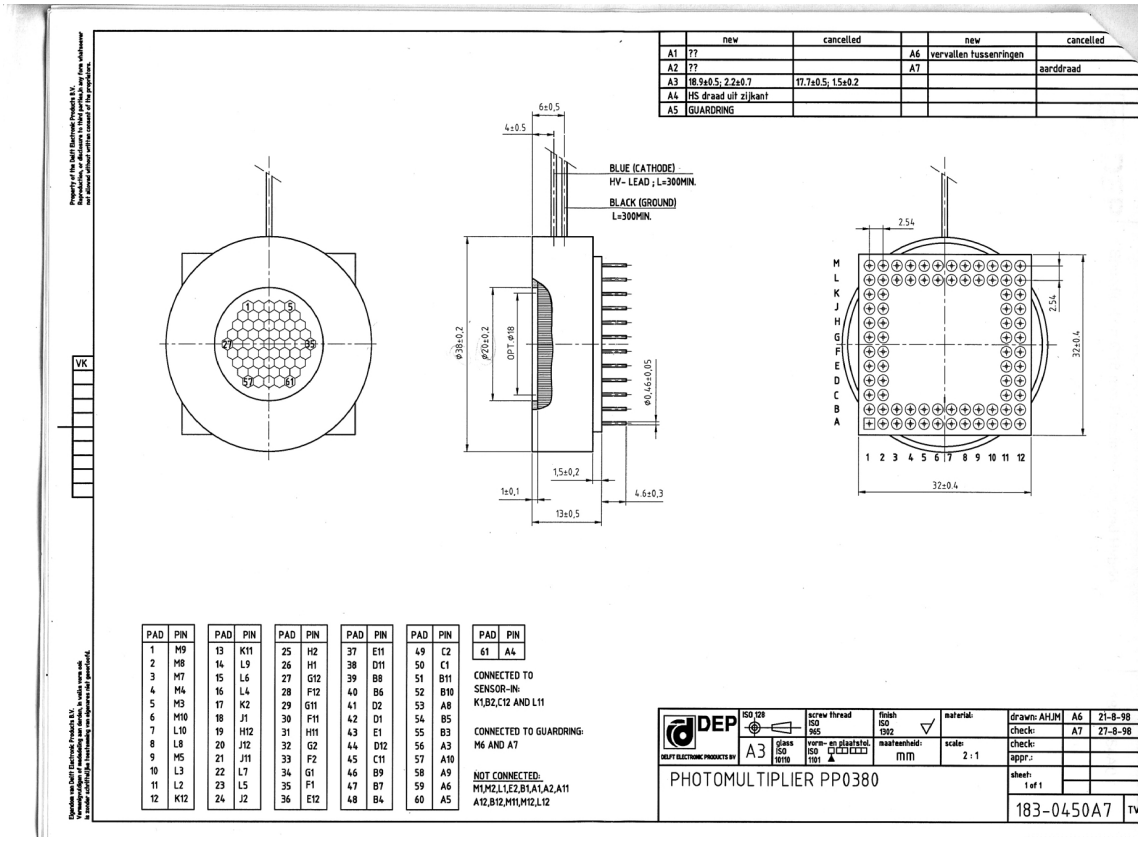


Figure 1: Design of the DEP 61 pixels HPD.

Table 1: HPD characteristics.

| | |
|---|---|
| Optical characteristics | |
| photocathode type | S20 |
| quantum efficiency (at 480 nm) | 16.7 % |
| quantum efficiency (at 520 nm) | 13.0 % |
| useful diameter | 18 mm |
| input window | fiber optics |
| operating voltage (max) | -12 kV |
| Electrical characteristics | |
| total active area | 225 $mm^2$ |
| number of pixels | 61 |
| flat to flat distance (hexagon) | 2 mm |
| diode active area per pixel | 3.5 $mm^2$ |
| gap between pixels | 50 $\mu$m |
| depletion depth | 300 $\mu$m |
| depletion voltage | 60 V |
| output capacitance | 4 pF |
| dead layer thickness (junction side) | 2 $\mu$m equivalent $Si$ |
| dead layer thickness (entrance side) | 0.1 $\mu$m equivalent $Si$ |

The setup used in Lyon to test the HPD is shown in Fig. 2. The HPD is plugged on a front-end board (9.5 cm × 12.5 cm) and kept in a metallic black box. The light can be distributed to the HPD either through a single 1 mm diameter clear fiber in contact with its entrance window or through a 61 pixels cookie matching the pattern of the HPD pixels (Fig. 2). This permitted us measurements of the cross-talk with a fiber-to-photo-detector connection very close to the final design. In particular one has to a) minimize the distance between the entrance window plane and the cookie and b) optimize the matching between the fibers and the HPD pixels. The second requirement is obtained by rotating the cookie and adjusting the light level on the illuminated pixel and the neighbours.


Figure 2: Left: HPD test setup in Lyon. The HPD is inside the metallic box. The clear fiber bundle is visible on top of this box. Also shown is the VA-DACQ acquisition system from IDEAS for the VA-TA readout. Right: details of the HPD cookie collecting fibers at the HPD entrance window. The hexagonal pattern matches the HPD pixel distribution.

We used LED ref. RS 235-9922 for the light source. This is the same with the one used by the MINOS collaboration for their calibration system [3]). The emission of the LED's (470 nm) is close to the maximum emission peak of the WLS fibers. The LED was driven with short pulses (around 50 ns width) of variable amplitudes and different repetition rates.

The high voltage supply must have extremely low ripple. We adopt the Matsusada [4] HV-15N-HP with 3 mV ripple for 15 kV. The bias voltage is provided by a floating power supply. These power supplies, as well as the front-end electronics digital and analog supplies, are controlled with low voltages.

## 2.1 Quantum efficiency

Quantum efficiency is obviously a key issue for the OPERA TT. The green extended S20 photo-cathode provides a high quantum efficiency (above 15 %) at the maximum emission peak of the WLS fibers. Fig. 3 shows the absorption and emission spectra of the Kuraray Y11 fibers, defined as the baseline WLS fibers for OPERA. Further these WLS have maximal attenuation length ($\sim 7m$) at the green. See Sect. 5.2.1 for detailed results.

Both these features offer some flexibility in the TT design. A good photon budget and low attenuation offer the possibility of putting the photodetectors at the corners (see Sect. 6).

The DEP specifications gave a quantum efficiency at the emission peak of the WLS fiber (480 nm) of 16.5 %. An independent measurement has been performed by J.Seguinot at CERN [5] who has kindly agreed to compare the quantum efficiencies of the Lyon HPD from DEP and the Lyon 64 pixel MaPMT from Hamamatsu. Fig. 4 shows the result of the measurement. At 480 nm the quantum efficiencies are quite comparable (15% versus 16.5%). The CERN measurements are in good agreement with the DEP specifications.

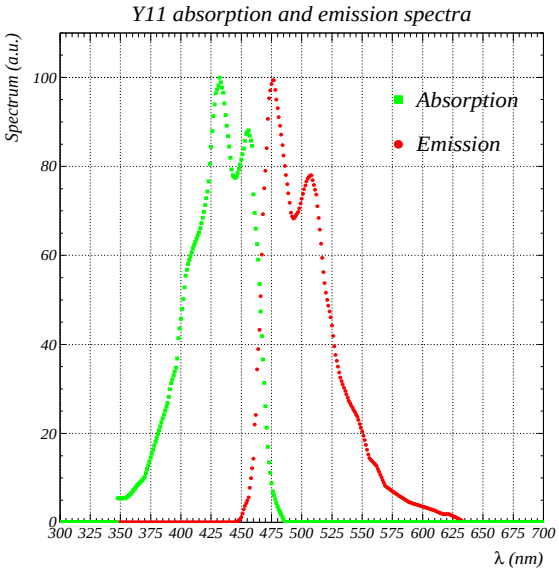


Figure 3: Kuraray Y11 WLS fibers absorption and emission spectra.

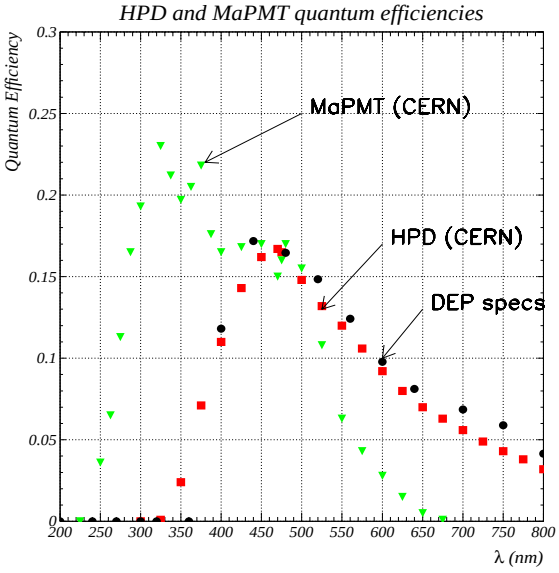


Figure 4: Quantum efficiency of the S20 photo-cathode measured by DEP (black dots) and by J.Seguinot at CERN (red squares). Also shown is the CERN measurement of the Hamamatsu 64 pixels MaPMT QE (green triangles).

One would have hoped to have a better ratio of the QE for the "multi-alkali" (HPD) over the "bi-alkai" one (MaPMT). The fact that they are comparable could be attributed to the difficulty of deposition on the fiber window, and the further losses that the the latter imposes on the incoming photons. DEP can guarantee photocathode efficiencies of the present range, but not 50% higher.

## 2.2 Resolution

HPD's are known to have excellent photon resolution. This is the consequence of the dissipative process in the silicon, responsible for the charge amplification. In a standard PMT, the multiplication in the first

dynode leads to strong fluctuations in the amplification and therefore a poorer resolution.

The resolution is illustrated in Fig. 5 obtained by flashing a given pixel of the HPD (used for triggering) with an average of 13 photo-electrons and looking at the signal on the 6 direct neighbours. Light was injected through a single clear fiber at a distance of roughly 1 mm from the HPD entrance window. The typical emission cone angle of the fiber used is $\pm$ 35$^o$.
Fig. 5 shows the result on the 6 neighbouring pixels and the detail of one of them. The photo-electrons are clearly visible and clearly distinct from the pedestal (first peak around 200 mV). At least 6 peaks are visible. The mean number of photo-electrons can be evaluated either with the mean value of the pedestal subtracted spectrum or with a Poisson fit to the distribution. Both methods give for this test an average number of 3 photo-electrons on all the pixels.

It is clear from figure 5 that the intrinsic resolution of the HPD gives an automatic calibration of the readout chain. The difference between two consecutive photoelectron peaks gives the gain (typically 60 mV/p.e with the front-end electronics used in these tests). Due to dissipative source of multiplication no gain variations are expected at the photodetector level.

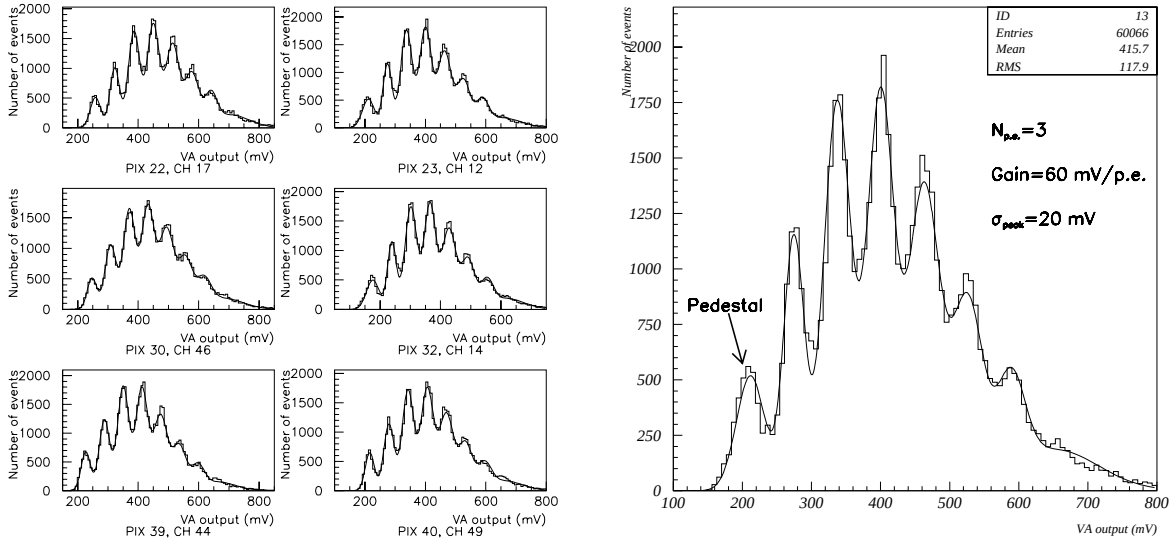


Figure 5: Left: light spectra on the six direct neighbours of a flashed pixel. Right: detailed spectrum of one of the pixels.

The HPD resolution of the single photo-electron has also been achieved in auto-trigger mode. The threshold of the electronics was set between the pedestal and the first photo-electron peak on the triggering part. We adjust this value on each pixel to compensate for pedestal spreads. Fig. 6 shows the dark current spectrum of the photo-cathode of one channel. The signal-to-noise ratio (around 6) gives an efficient separation between pedestal and first photo-electron peak. Since one triggers on a part of the signal shaped with a fast amplifier the noise is higher at the trigger part than at the charge-measuring part and the good signal to noise ratio of fig 6 does not mean that we trigger with a 100% efficiency. The auto-trigger efficiency, is currently under study (see 3).

## 2.3 Linearity

We studied the evolution of the HPD gain as a function of the high voltage applied. This test was performed by recording the dark current spectrum for various high voltages. The minimum high voltage value to separate the first photo-electron from the pedestal is 5 kV. The maximum high voltage applied was 10 kV. The positions of the two peaks are given by the mean values of two gaussians. The theoretical gain slope is 1000/3.62 = 276.2 e$^-$ per kV. The result of the measurement is displayed on Fig.7 with a fitted slope of 268 e$^-$ per kV in excellent agreement with the previous estimation.

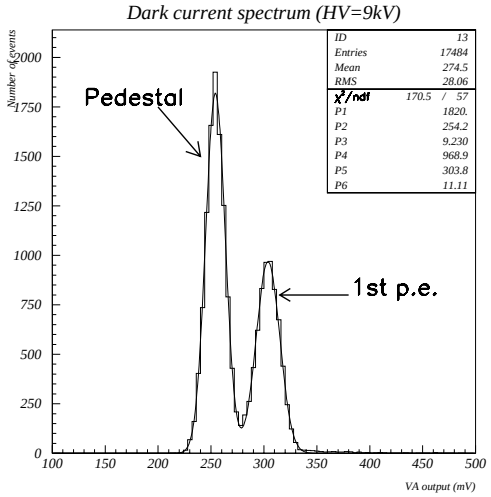


Figure 6: Dark current spectrum obtained in auto-triggerable mode

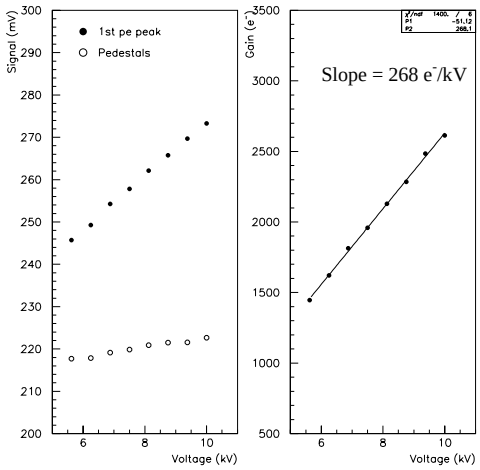


Figure 7: Left: Positions of the pedestals and the first photo-electron peak as a function of the high voltage applied to the HPD. Right: Evaluation of the gain for each high voltage applied.

## 2.4 Uniformity

The pixel-to-pixel gain uniformity is a clear advantage of the HPD. The uniformity is important for the front-end electronics design that has not to take into account the gain spread compensations.
We measured the uniformity with the dark current spectrum for every pixel as explained in the previous subsection. We operated in auto-triggerable mode with a threshold adjusted between the pedestal and the first photo-electron peak. The high voltage applied was 10 kV. The gain obtained was then corrected with the variations in gain of the front-end electronics determined independently in a charge calibration mode. The result is shown in Fig.8. The left plot displays a 2-D view of the 61 HPD pixels with their gain (in electrons). The right plot gives the distribution of the single photo-electron charge $Q_{pe}$ for the 61 pixels. The resulting gain non-uniformity, defined as $\sigma_{Q_{pe}}/\langle Q_{pe}\rangle$ is less than 5% .

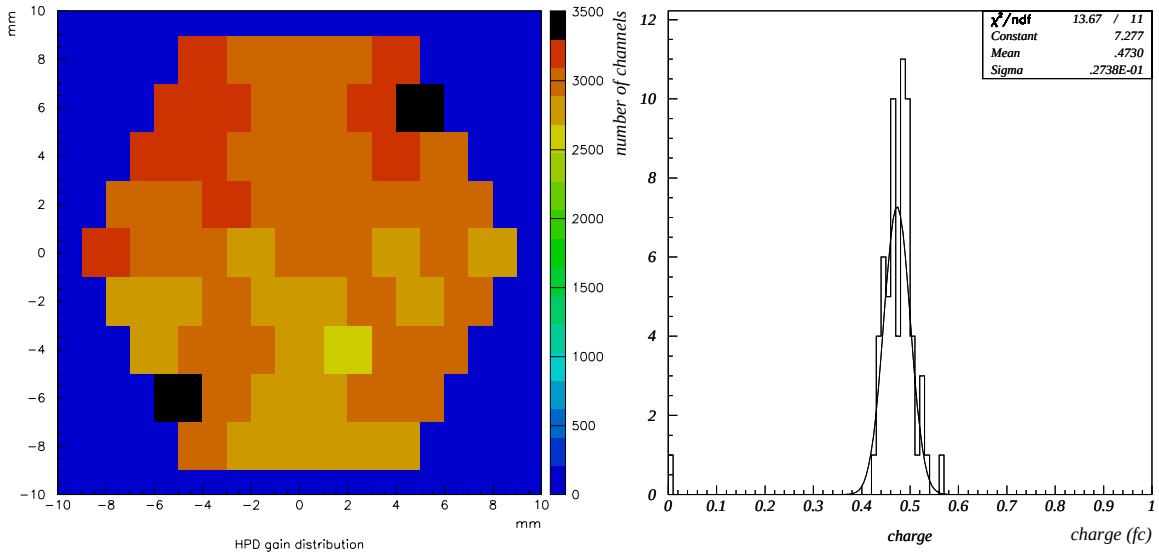


Figure 8: Left: projection of the gain (in electrons) for the 61 pixels of the HPD. The gain spread ranges from 2500 to 3500 electrons. Right: single photo-electron charge distribution.

## 2.5 Cross talk

We evaluated the optical cross-talk of the HPD by illuminating a pixel with a clear fiber in contact with the entrance window. The light injected had an average of 6 photo-electrons. No optical grease was used. The cross-talk is given by the fraction of signal received by the neighbouring pixels.
The Fig. 9 shows the 3-D view of the signal received by the 61 HPD pixels, normalized to the signal of the flashed pixel. The maximum signal correlated with the light injected is recorded on the 6 direct neighbours of the flashed pixel and is not larger than 2% per pixel. This intrinsic low cross-talk is obtained thanks to the fiber optic entrance window which gives a better focalisation of the incoming light.

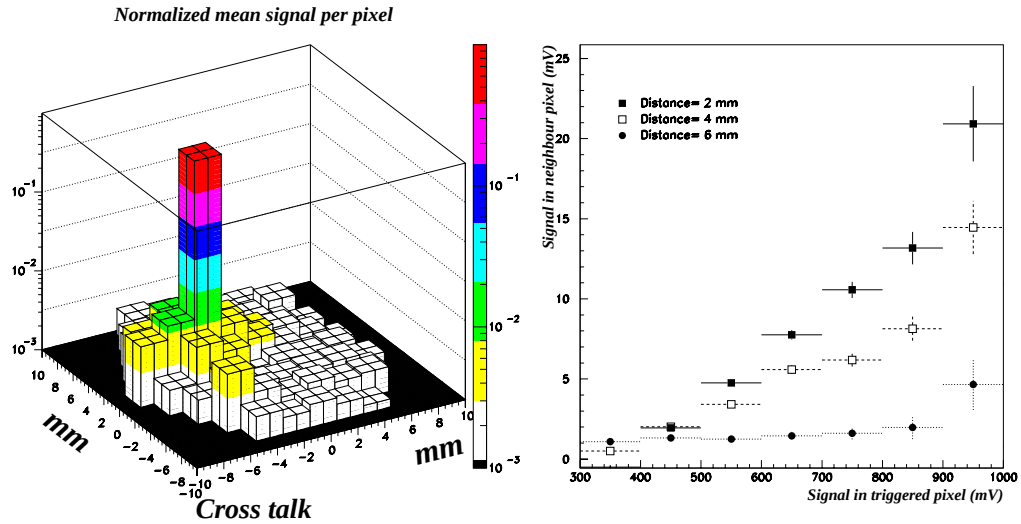


Figure 9: Left : 3-D view of the signal received by the HPD 61 pixels, normalized to the maximum signal. The maximum cross-talk signal is less than 2%. Right : distribution of the light received by a pixel w.r.t. the distance from the illuminated pixel.

## 2.6 Dark current

The corollary of the sensitivity at large wavelengths is the increase of the dark current (thermo-emission of the photo-cathode). This dark current must be kept at a reasonable level in order to minimize the dead time in an auto-triggerable acquisition operating with a threshold of a fraction of photo-electron (see Sec. 7 for detailed results).

Two different measurements have been performed to cross-check the dark current rate with the one given by DEP specifications. The first one is a direct measurement of the dark current spectrum in auto-trigger mode with a threshold below the first photo-electron. The limitation of such a measurement is the uncertainty on the trigger efficiency at any given threshold. A second measurement has therefore been performed with an external trigger by looking at random dark current counts occurring in correlation with the external trigger. Indeed the number of such events is given by : $N = f_{DC} \times f_{external} \times T_{integration}$, where $f_{DC}$ is the dark current rate, $f_{external}$ the external trigger rate and $T_{integration}$ is the time of sensitivity of the electronics (typically few $\mu$s). The parameter $T_{integration}$ and the cut applied to select events corresponding to single photo-electrons have been cross-checked with a LED spectrum (pulsed light at a frequency equal to $f_{external}$)). Fig.10 shows the different spectra obtained with such a method.

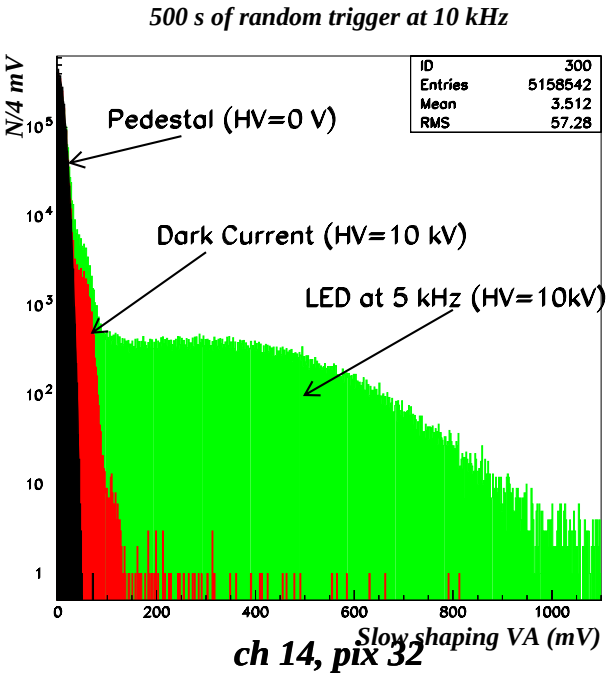


Figure 10: Light and dark current spectra obtained with an external trigger. The light spectra is used for calibration. The dark current events are in the first photo-electron peak.

Both measurements are consistent with a dark current rate around 25 kHz cm$^{-2}$ or 1 kHz/pixel. It should be emphasized that the HPD was inside its closed metallic box and the temperature was typically $T_{ambiant} + 5^o$. The results obtained in Lyon are consistent with DEP specifications (14 kHz cm$^{-2}$) given the uncertainties on the temperature conditions (the dark current may double every 5 degrees).

This high value of dark current rate is clearly unacceptable. DEP agreed to test a a new type of S20 photo-cathode, the so-called "hot" S20, with same features around 500 nm but lower sensitivity in the red (see fig 11) . The specifications for the dark current are below 4 kHz cm$^{-2}$. This new photo-cathode is available on the 61 pixels version and is also the photocathode used by the new multipixel HPD: the 163 pixels HPD (see Sec. 6 for details). Given the lower size of the pixels in this new HPD, the dark current rate should decrease to an acceptable rate below 65 Hz per pixel. A new 61pixel HPD with "hot S20" photocathode has been delivered and will be tested shortly.

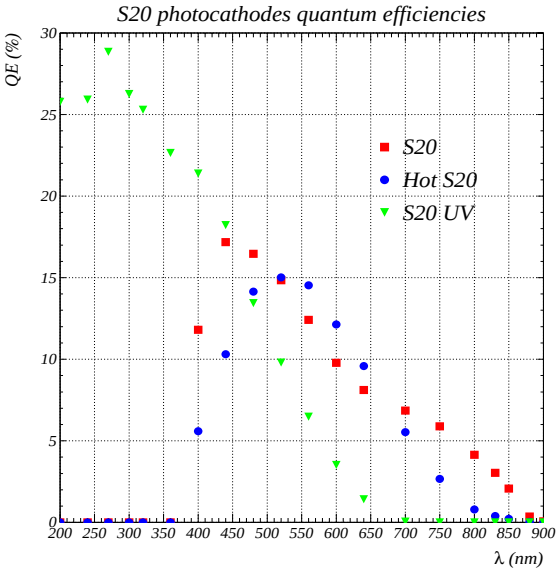


Figure 11: Left : quantum efficiency of the S20, "hot" S20 and S20 UV photo-cathodes as measured by DEP. The S20 UV photo-cathode may be deposited on a quartz input window only.

## 2.7 Advantages and limitations of the HPD for OPERA

The HPD advantages have been presented in detail:

- Excellent resolution (S/B above 6) permitting autocalibration of gain
- Excellent uniformity (2%) and linearity (1%)
- Very low cross-talk (2%)
- Immunity to magnetic fields. Though this might be less relevant for OPERA

The two "weak" points of the HPD are:

- the high rate of dark current (1 kHz/pixel), a deficiency that will be hopefully corrected by the new photocathode the "hot S20" (65 Hz).
- the low gain, imposing sophisticated electronics. This we consider a less severe problem. We believe that the new generation of low noise electronics is sufficiently well understood permitting us to tackle this problem with sufficient confidence. In fact we have shown in the previous subsections results on the single photoelectron detection. Further the experimental levels of noise achieved (see 3), show that the fully efficient single photoelectron detection is not out of reach.

# 3 The front end

## 3.1 The VA-TA principle

The front-end electronics belong to the VA-TA family, first developed at CERN under the name VIKING [6] and produced by IDEAS [7]. We briefly recall its principle: the VA-TA's are multi channel chips[2], with charge-sensitive preamplifiers followed by a fast and a slow shaper. The slow shaper (VA) has a peaking time of 1-2 microseconds and the fast shaper (TA) has a rise-time of $\sim$ 75 nanoseconds. Each channel in the trigger chip TA is followed by a level-sensitive discriminator with adjustable threshold, a serial shift-register to select the channels allowed to trigger and a monostable. In the VATAcg version a different threshold can be set for each channel. The outputs are ORed together and can be sent to the VA part. The OR then serves as a sample and hold signal for the charge accumulated at the VA part. The delay between trigger and hold matches the peaking time of the VA ($\sim 2\mu$s). The same OR signal can initiate the readout sequence. In the VA part, the outputs of the preamplifier enter a multiplexer. Its switches are controlled by a bit-register running in parallel. The output of the multiplexer goes to the output of the chip via a buffer. Only one of the channels is seen on the output at every readout step. The speed of readout is then limited by the multiplexer clock which makes the bit in the register toggle from one channel to the next. The specifications for the maximum acceptable clock frequency give 10 $MHz$, though we encountered problems when trying to read above 5 $MHz$. The data can then be clocked into an ADC.

The chip can also be operated in test mode via another multiplexer/bit-register on the input, injecting charges in the preamplifier inputs. Further, it is also possible to use an external trigger for the VA sample/hold and the start of the readout sequence. We will report below on tests where we have used both an internal and an external trigger.

The working principle and the timing sequence of a VA-TA combination are displayed in Fig. 12.

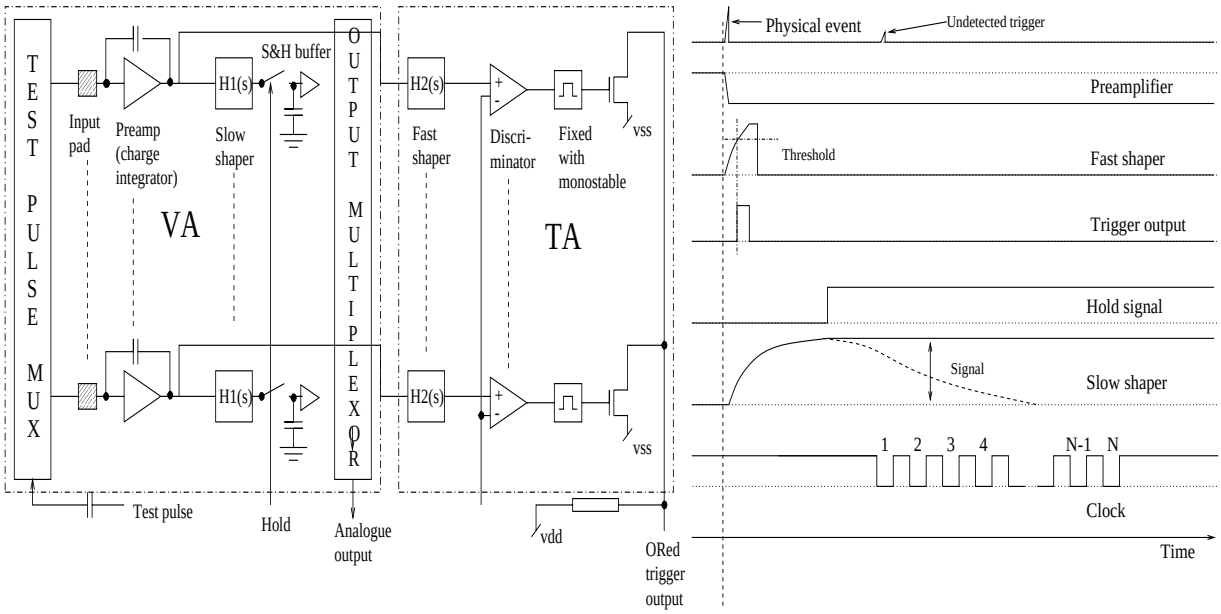


Figure 12: Working principle and timing sequence of the VA-TA.

Given the low gain of the HPD (3000 $e^-$ per photo-electron) the VA-TA should have high gain and low noise performance. These characteristics have been investigated either in test mode (with injection of charge via a 1.8 pF capacitance) or directly with the HPD connected. We have also characterized the chips in term of dynamic range, peaking times and common mode noise.

[2]There are versions of 32, 64 and 128 channels

## 3.2 3 different VA-TA

The VA-TA concept can be applied both to HPD and MaPMT. One has to adjust the polarity of the input signal and the dynamic range of the chips. For the HPD readout, we use the so-called VA32c and VA32rich. The first one has a good signal/noise ratio but a very limited dynamic range (linear on the ± 11.5 fC range, corresponding to a maximum light yield of 46 photo-electrons). The second one has a larger dynamic range (linear from -65 fC to +65 fC, corresponding to 260 photo-electrons). For the MaPMT readout we can use the the VA32hdr11 chip (hdr standing for high dynamic range). Although the general features of this chip are comparable to the one of the former chips, its dynamic range is considerably larger and matches the characteristics of a PM signal (from -25 pC to +25 pC). All these chips were bonded directly with a TA32cg chip for triggering.

The comparative data for the VA32c, VA32rich, VA32hdr11 and TA32cg are given in Tab.2. Due to lack of time we were able to test fully only the VATAcg chip.

Table 2: VA-TA performance.

| Chip | VA32c | VA32rich | VA32hdr11 | TA32cg |
|---|---|---|---|---|
| Gain(mV/fC) | 150 | 35 | 0.1 | -16 (Gain stage=10) |
| Noise (mV) | 10 | 1 | 0.25 | 2.5 |
| Peaking time ($\mu$s) | 2 | 2 | 0.8 | 0.075 |
| Dynamic range (± fC) | 11 | 65 | 25000 | |

## 3.3 Performances of VATAcg

### 3.3.1 Gain

The gain is measured in calibration mode. Symmetric measurements are performed for the VA and TA chips. For the VA chip, the pulse-height is recorded for different values of injected charge. This gives the value of the pedestals and the gain. For the TA, a scan is performed over the threshold voltage range for a given calibration charge. The threshold is found when the 50% trigger efficiency is reached. The repetition of the procedure for different calibration charges allows the determination the gain of the chip. The symmetric procedure may also be used for cross-check (scan of the charge range for a given voltage threshold). Both procedures lead to similar results. The TA32cg chip has a gain stage that can be adjusted externally. This stage allows to select variable gain in the approximative ratios 1:3:6:10. The distribution of the gains for two VA32c and two TAcg chips are displayed in Fig. 13. The mean value for the VA(TA) is around 120(-16) mV/fC and the gain spread/chip is around 2%. The pedestals remain stable when the HPD is connected and the HV is applied.

### 3.3.2 Noise

The VA noise is computed from the fit of the pedestal distribution. The distributions for two VA32c chips, without common-mode noise subtraction, are given in Fig. 14. They are around 10 mV corresponding to 500 $e^-$ ENC. The intrinsic noise of the chip (obtained before connecting the HPD) is of the order of 200 $e^-$ ENC. The TA noise is computed from the trigger efficiency curve. A typical distribution is shown in the same figure. It is around 2.5 mV corresponding to 900 $e^-$ ENC. From standard theoretical curves of noise versus sampling time one knows that a factor of 2 reduction in noise for both the VA and the TA is possible (200 and 500 $e^-$ ENC respectively for the VA and the TA); provided an optimized PCB is designed. For the VA, the performances as they are now are sufficient, but a reduction in noise of factor 2 would certainly be more than welcome in the TA part.

### 3.3.3 Trigger

The TA gives a trigger that is common for all the chip. The threshold is also set for all the TA channels. The channel-to-channel spread becomes a limitation when we are dealing with very low thresholds. To overcome this behaviour, a 3 bits DAC has been implemented in the chip to allow individual adjustment

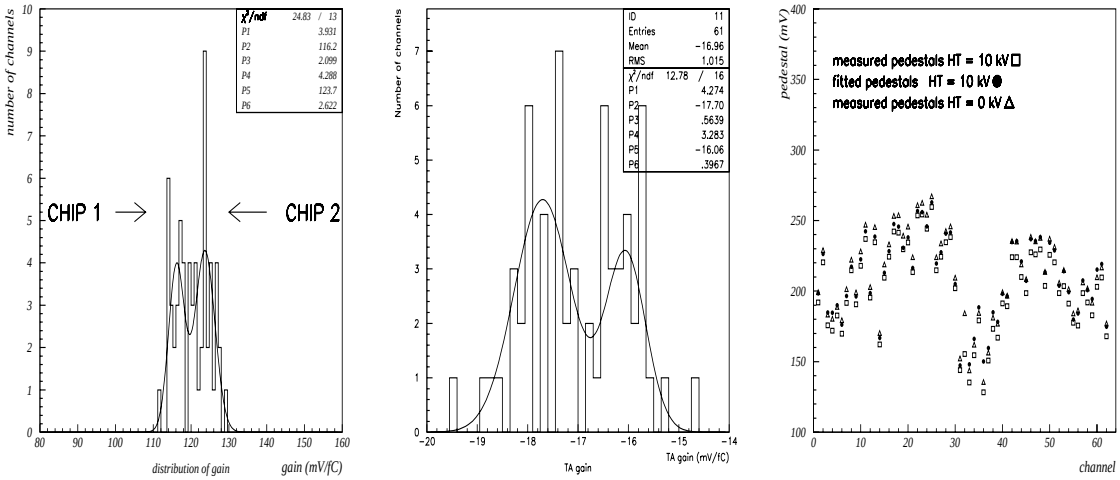


Figure 13: Distribution of the VA32c gain (left), TA32cg gain (center) and VA32c pedestals (right). The last plot shows the stability of the VA pedestals when we connect the HPD and apply the high voltage.

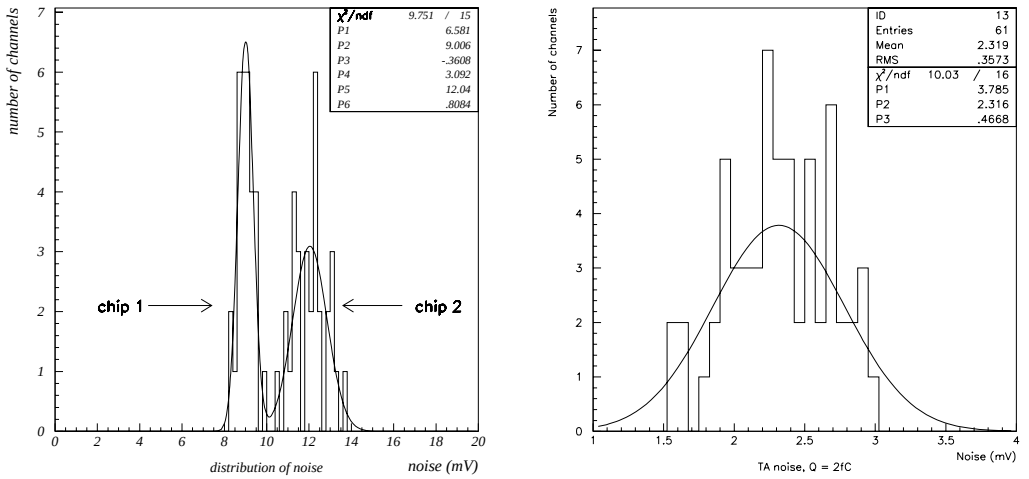


Figure 14: Distribution of the VA32c (left) and of the TA32cg (left) noise. The variation of the noise w.r.t. the peaking time is also shown (right).

of the thresholds around the common value. The threshold spread is then reduced by a factor 3 after optimization of the bit-pattern in the DAC mask (Fig. 15)

### 3.3.4 Dynamic range

The linearity of the front end electronics over the full required dynamic range ($1 - 200\,p.e.$ corresponding to $0.5 - 100\,fC$) can be checked in the calibration mode.

The signal of the VA as a function of the input charge determines the dynamic range. The data are well fitted by a polynomial of order three $VA_{output} = a_0 + a_1 Q + a_2 Q^2 + a_3 Q^3$. Fig.16 shows the data of the signal and the fit as a function of the input charge. The VA32C has a linear dynamic range from $0fC$ to $12.5fC$. For higher values, the difference between a linear and a polynomial (of order three) response becomes important, but acceptable and can be corrected up to 20 $fC$. With minor modifications the chip can accept only one polarity and therefore double its range up to 25-40 fC corresponding to 80 p.e. But this is not the direction we have taken, since we intend to test the VA-rich chip which has a much higher dynamic range (230 p.e).

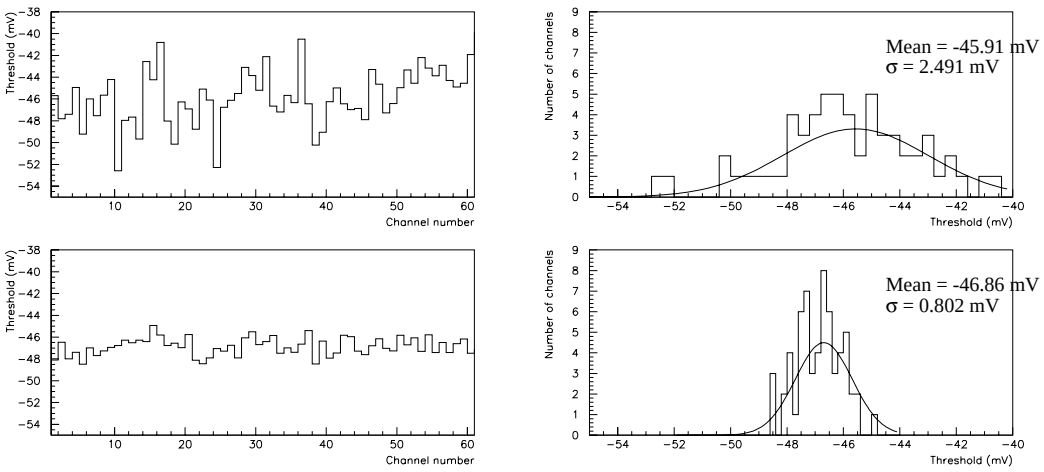


Figure 15: Reduction of the threshold spread after DAC optimization in the TA chip.

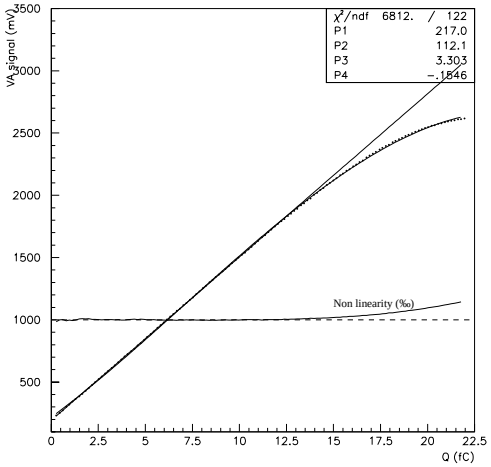


Figure 16: Linearity range of the VA32c signal.

# 4 ORCA a readout card for OPERA

During the beam tests of May and June 2001 we completed the first tests of a full readout chain, from the scintillator to the workstation, in what we propose to be the final configuration. The results of these tests will be presented in the next section. In this section we present the acquisition card, under the preliminary name ORCA (Opera Readout CArd) which includes a 12bit, 25 MHz ADC, the sequencing element (a FPGA of the type Altera APEX 20K200) and an Ethernet chip porting the data directly to a PC. The Ethernet controller (currently a 10 Mbits/s HP chip to be soon replaced by a 100 Mbit/s LINUX chip) allows not only to access and control the front-end electronics through *http* performing slow control functions but also send the data through *TCP/IP* [8] to the workstation with high throughput (for the time being: 1 Mbit/s). The design, development, production and testing of ORCA has been done by our laboratory.

A block diagram of ORCA and its interaction with the VATA front-end is shown in figure 17

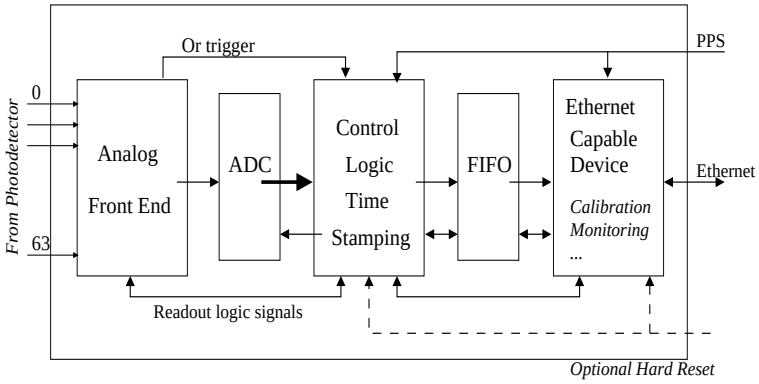


Figure 17: Schematics of an Ethernet Capable Front-end Module

This card allows a direct control of the acquisition without using an acquisition bus. It is cost effective, given the low price of the Ethernet controller chips, easy to control from a PC under Windows or Linux and well suited for a complete integration close to the front-end electronics since only one Ethernet cable is needed to access the acquisition. It is also a perfectly flexible candidate for testing the scintillator modules at different labs during the production phase, and during installation at Gran Sasso, since it is perfectly autonomous: any portable PC can be connected to the Ethernet port and take data.

A photo of the card can be seen in figure 18.

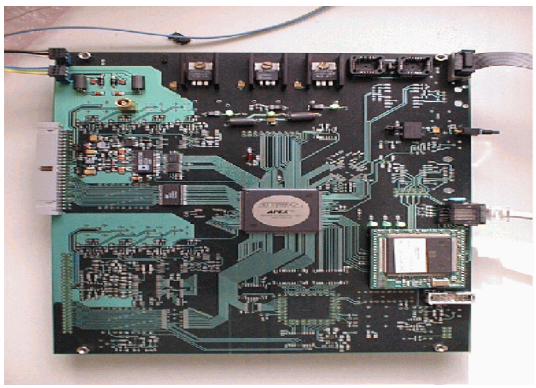

Figure 18: The ORCA module

## 4.1 The concept of an Ethernet Capable Front-end Module

ORCA, in more detail, is an Ethernet Capable Front-end Module using a Ethernet device from Agilent Laboratories [9] (Webplug or BFOOT 11501). This device is a custom ASIC based on a 68000 microprocessor and the VxWorks real time kernel. It contains an embedded Ethernet controller, including a Web server and expects to receive the front-end data through a 5 Mbps link obeying the IEEE 1451.2 standard [10]. The IEEE 1451.2 standard provides the ability to produce network-capable "smart sensors". It partitions a smart device into a Network Capable Application Processor (NCAP, in our case the BFOOT) and a Smart Transducer Interface Module (STIM, in our case the ADC with the FPGA sequencer). The STIM architecture includes two main blocs. The first bloc implements the minimal mandatory part of the IEEE 1451.2 standard. The second main bloc contains the transducer channels and the front-end sequencer. This bloc provides all the features needed to control the analog front-end chip (VA-TA32cg). The NCAP processor interfaces the STIM with the Network and allows to control it transparently.

The present prototype includes a time stamping function, realized by latching an external signal and giving it a time label coming from a local clock. A dedicated inpu from an externally distributed clock synchronized on a GPS receiver permits an absolute time stamping.

A node can be accessed in a variety of ways.

- The primary method is through the web interface by typing a Universal Resource Locator (URL). Fig. 19 shows an example of JAVA applet which can read continuously an ADC channel in an oscilloscope mode.

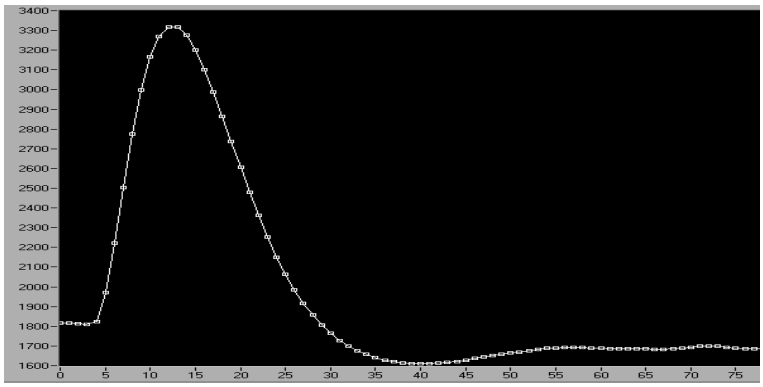


Figure 19: Web Oscilloscope

- The node can also be accessed by http commands. E.g the command: **Http ://ly-otmp9/bin/1451dot2/read ?startChan=2&stopChan=2&stim=1** reads a channel with 2 bytes of data.

- The BFOOT also provides a data streaming application which allows to keep a network connection opened and send the data continuously on Ethernet. The data streaming mode is a specific application based on two threads, which share the same set of ring buffers. We have achieved throughput close to 1 Mbit/s with this function. Figure 20 shows an example of data taken through the network.

We validated the concept using the embedded Ethernet controller BFOOT 11501. Unfortunately, Agilent has decided to discontinue this chip due to insufficient demand. We luckily found its successor, a low power processor (less than 500 mW), implementing full LINUX capabilities, including multitasking and equipped with a 100 Mbit/s port. It is called ETRAX [13] and has had a very wide distribution (over 1 million sold already). Choosing a processor with LINUX, is a guarantee that we will be immune to industrial accidents of the type experienced already with Agilent.

## 4.2 May-June beam tests: test of the full readout chain

In the basic module used for the tests (see Fig. 21) the card was fixed between two parallel metallic planes. The connection to the front-end electronics (power supplies, biases, digital signals and outputs)

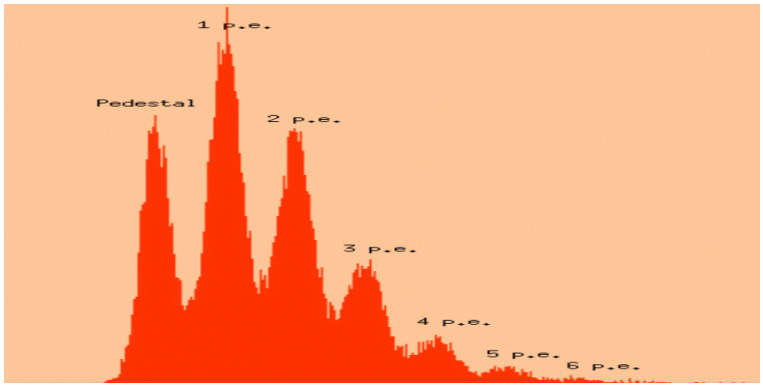


Figure 20: Example of a data acquisition through the Ethernet

was achieved via a 50 pins ERNI connector and a flat cable (this was imposed by the front-end electronics board). The HPD, plugged on the front-end board, was inside a small metallic box shielded against light leakages. All the power supplies (high voltage and HPD bias voltage) were fixed on the back side of the module. The module was then driven by low voltage signals (max +24 V) controlled from the control room and the data acquisition was performed through a single ethernet connection. This gave us a high mobility and flexibility of installation and running.

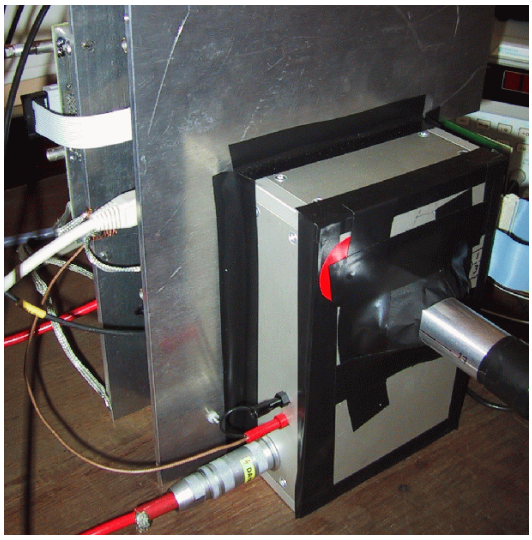

Figure 21: Picture of the HPD/VA-TA/Ethernet DAQ module used during the May and June tests beams at CERN. The HPD with its front-end electronics is located in the metallic box. The DACQ card is sandwiched between the two metallic planes. Power supplies are attached on the back-plane.

We tested the control of the front-end electronics both in external and in auto-triggerable modes. We checked the data transfer up to 1 Mbits/s (corresponding to 150 Hz/channel event rate for the 64 channel VATAcg). We also checked the timestamping and labeling of the events. The triggers (external and auto-trigger) were timestamped thanks to a local 50 MHz local clock (20 ns accuracy) to allow for off-line reconstruction.

The data transferred were the ADC value(s) for 1 to 64 channels, the trigger timestamps and also two different types of counters giving the number of auto-triggers between two external triggers and the number of auto-triggers in a given time window after the last external trigger. These two counters are used to study noise and trigger efficiencies. All the functionalities of the readout chain have been successfully tested. Data presented in the next section were obtained with this readout system.

The setup of the readout chain used in May-June tests is illustrated in Fig. 22.

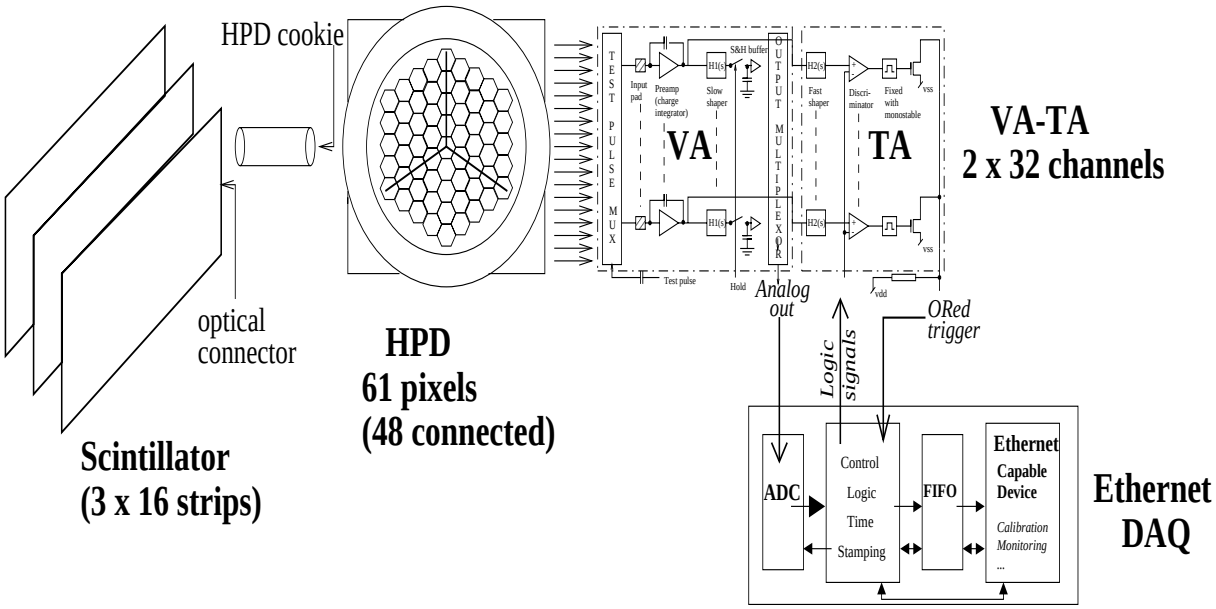


Figure 22: General architecture of the scintillator telescope readout chain. The major elements of the chain are the detector itself, the HPD, the VA-TA front-end chips and Ethernet DACQ system. The full chain was tested during the May and June beam tests period.

# 5 HPD tests with plastic and liquid scintillator

We performed tests of scintillator readout with an HPD, using both plastic and liquid scintillator with radioactive sources, cosmic rays and particle beams.

## 5.1 Tests of the HPD with the plastic scintillator

### 5.1.1 A small telescope prototype

A small plastic scintillator prototype was built in Lyon. The prototype has 3 planes of 16 plastic scintillator bars. The scintillator came from Pol.Hi.Tech (same batch as the one used to build the full scale prototype in Strasbourg [11]). The bars were 41 cm long, 2.6 cm wide and 1 cm thick. Each bar is read by WLS fibers. Two planes were equipped with Kuraray Y11 fibers (1.2 mm diameter) and the third one has Bicron BC91A fibers (1 mm diameter). The WLS fibers end to an optical connector at both ends. They are glued to this connector with carbon doped glue. The ends of the fibers are then polished by hand. The minimal and maximal fiber lengths are respectively 70 cm and 100 cm. The fibers are glued to the scintillator in a groove (1.6 mm thick and 1.6 mm deep) made with a saw. The glue is the standard Bicron BC600. The bars are then painted with a reflective paint. We used the Bicron BC620 and applied 4 layers with a brush. The strips are then collected, glued together in a 70 cm $\times$ 41 cm U-shape aluminium profile (the aluminium thickness is 500 $\mu$m). The optical connectors are also glued on this profile. The plane is then closed with another U-shape aluminium profile glued to the first profile and to the strips (Fig. 23).

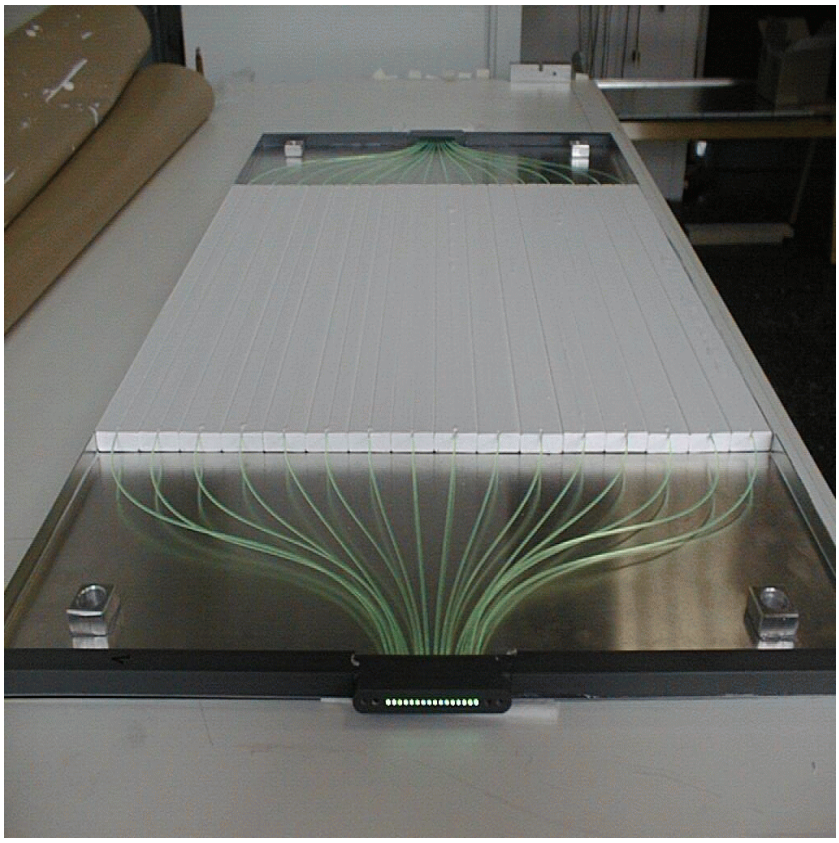

Figure 23: View of a scintillator plane with strips glued on an aluminium profile and the WLS fibers ended by the first half of an optical connector.

The three planes can be aligned thanks to transverse bars fixed with screws. The distance between planes can be varied (Fig. 24).

Figure 24: View of the three telescope planes.

### 5.1.2 Connector transmission and crosstalk

In the tests of May and June 2001 at CERN the light was read on one side by a single HPD with 48 pixels connected. The transmission was ensured by a bunch of 35 cm long clear fibers (Bicron BC98MC, 1.2 mm diameter) ended on the telescope side by an optical connector, matching the one of the scintillator plane, and on the photo-detector side by a hexagonal cookie matching the HPD pixel pattern.

The strip-to-clear-fiber connectors have been designed and built in Lyon. They consist of two PVC pieces, 68 mm large and 10 mm wide with 16 holes for the fibers, two 3 mm diameter holes for the alignment pins and two 3 mm holes for the screws. Two consecutive fibers are separated by a 2.5 mm gap. Fig. 25 give the details of the optical connector.

The relative alignment of the two halves is given by two metallic pins. The mechanical accuracy of the fibers holes is supposed to be at the level of $\pm$ 20 $\mu$m. The surface of the two halves has been polished by hand. The overall transmission of these connectors has been measured to be above 80 %. It can in principle be increased with a harder material (PVC used to get some deformations if one press the two halves too hard), optical grease and also by a different treatment of the surfaces (with a diamond fly-cut machining for instance).

On the cookie side we made "Mercedes like" cookies to merge the 3 16fiber bunches to the same HPD, testing the possibility that the granularity of the detector does not match the granularity of the strip module, or the strip connector. The non-connected pixels were covered with black adhesive to minimize possible reflection of light at this end. We have also constructed similar cookies for the MaPMT's (see Fig. 26. They will be used in comparative tests.

### 5.1.3 MIP response

Tests have been done in CERN (PS T7) in May and June 2001. The first calibration test is the measurement of the MIP response. The telescope was put on a movable $x$-$z$ stage (from Bern University) so that we could scan the response strip by strip. We operated with an external trigger defined by the coincidence

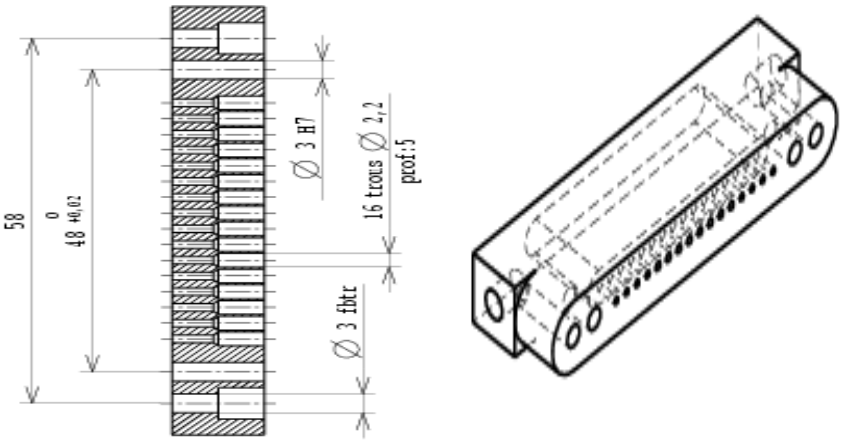


Figure 25: Views of the two optical connector halves : clear fibers side (left) and WLS fibers side (right).

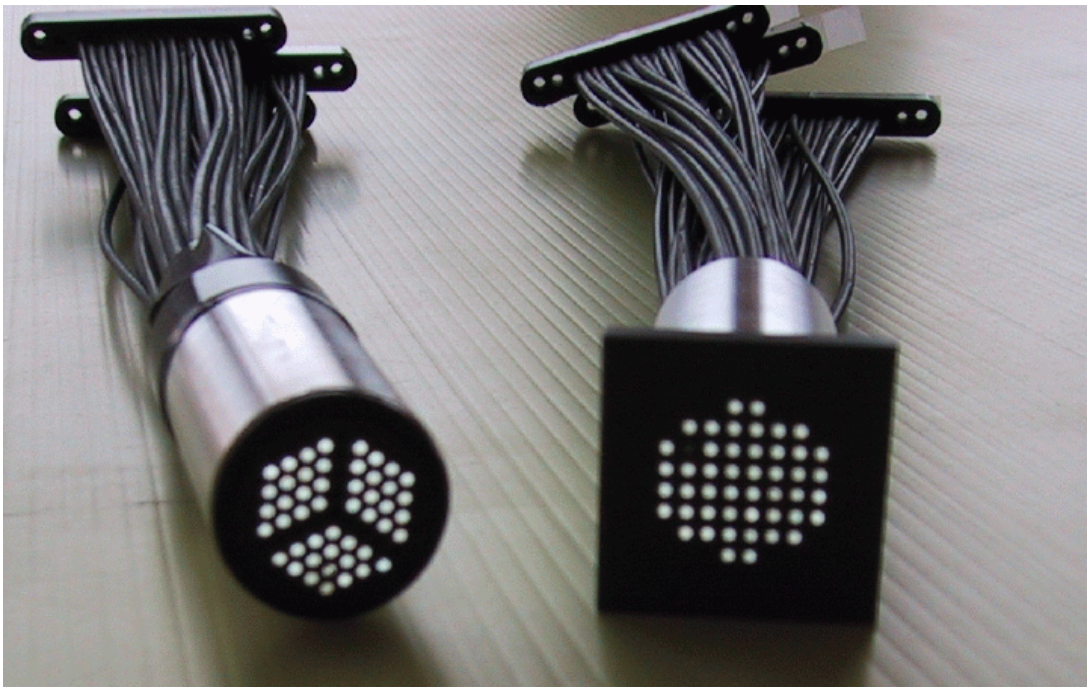

Figure 26: Picture of the HPD (left) and MaPMT cookies (right) connected to the plastic scintillator telescope.

of 4 scintillators (2 of them were 1 cm wide fingers). We run with 10 GeV particles (mostly pions with a small amount of electrons). The response of the strips is displayed on Fig. 27. Two estimations have been performed, the first one using a Poisson fit to the distribution and the second one relying on the mean value of the distribution. Discrepancies between the two estimations occur for some strips (mainly in the plane with 1 mm fibers) because of large pedestals on the corresponding channels that give a lower than expected mean value. Another limitation in the systematic scan of the MIP response was the low statistics for the strips at the edges (mainly strips 15 and 16). The average number of photo-electrons obtained on the planes with 1.2 mm WLS fibers is 8.4 for the first plane (with a RMS of 0.8) and 9.0 for the second one (with a RMS of 1.3). The corresponding number of photo-electrons for the third plane is 6.1 (RMS 1.2). This lower value is mainly due to the lower light yield of the BC91A fibers compared to the Y11. One fiber was broken at the edge of the plane. The results obtained here are consistent with those obtained on similar distances with the prototype in Strasbourg.

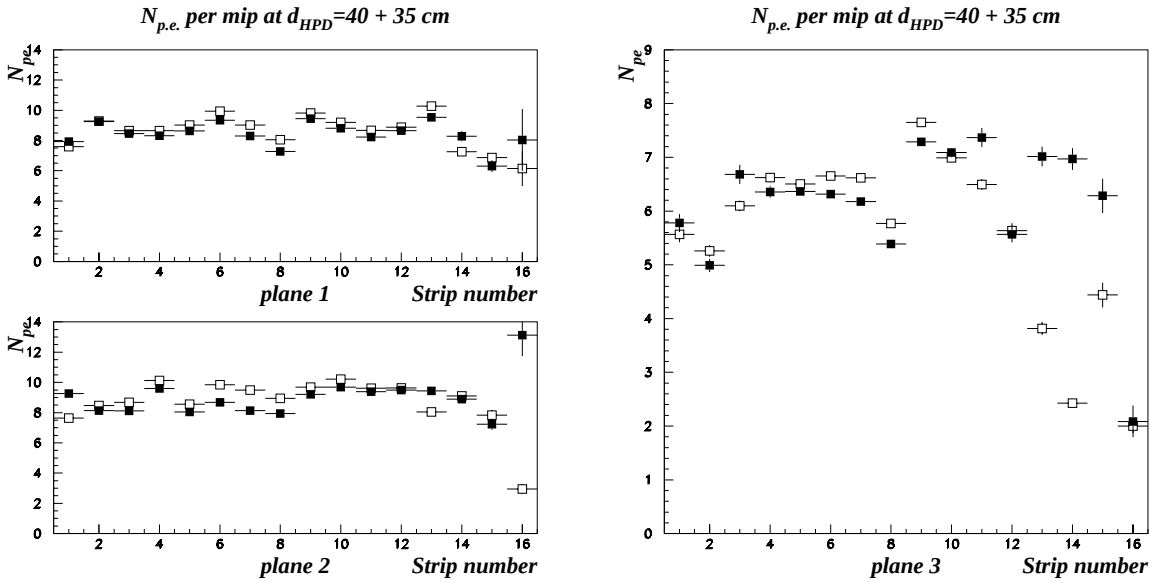


Figure 27: MIP response of 32 strips equipped with 1.2 mm WLS fibers (left plots) and with 1 mm WLS fibers (right plot). The average number of photo-electrons is respectively 9 and 6 for the two fiber diameters. Fiber # 16 on plane 3 is broken.

### 5.1.4 Optical cross-talk

The optical cross-talk with the HPD cookie has been studied as well. As mentioned before, one has to optimize the position of the fibers w.r.t. the position of the HPD pixels. This is done by rotating the cookie around the central fiber to maximize the signal on one given pixel and to minimize the signal on the neighbours. This procedure gives a satisfactory cross-talk below 2% (which is the intrinsic limit of the HPD). Fig. 28 shows the cross-talk for the events occurring in pixels 13, 24 and 42 (corresponding to the strips # 8 in each plane). The fraction of the incident light is less than 2% on the neighbouring pixels of these 3 pixels.

## 5.2 Tests of the HPD with the liquid scintillator

Tests have also been performed using liquid scintillator setups. The detectors have been produced at CERN (by I.Kreslo and collaborators). They consist of polycarbonate cells ($1 \times 1$ cm$^2$ cross-section) of variable lengths (up to 7 m) filled with Bicron BC570 scintillating oil. The light is read by a 1.2 mm WLS fiber (Y11) which is located approximatively at the center of the cell. Each cell is closed by a $\sim 3$ cm silicon joint (CAF50 silicon glue). We first tested with cosmic rays a 12 cells detector (4 planes of 3 cells) 6 m long, read on one side by the HPD, without any reflector on the other side. In this detector, the cells were not closed and the liquid came down to the HPD cookie . Then we took data on the full scale liquid scintillator prototype at CERN during the May and June beam test period. The $TiO_2$ load was increased to 20% between the two tests to improve the light yield and decrease the optical cross-talk between adjacent cells.

### 5.2.1 Cosmic ray setup. Measurement of attenuation length

The cosmic ray setup described above is shown on Fig. 29. The detector was wrapped with aluminized Mylar. The triggering system consists of 3 PM's in coincidence and the trigger was send to the HPD readout system. The 12 fibers were connected to an HPD through a specially made cookie.

The aim of this test was to measure the attenuation length along the fiber. Data have been taken at different positions along the detector (from 0.6 m to 5.8 m) by moving the triggering system. The average number of photo-electrons at 4 m was measured to be 5. Fig. 30 shows the variation of the light yield w.r.t. the distance to the HPD. Given the low statistics (each point corresponds to $\sim 24$ hours

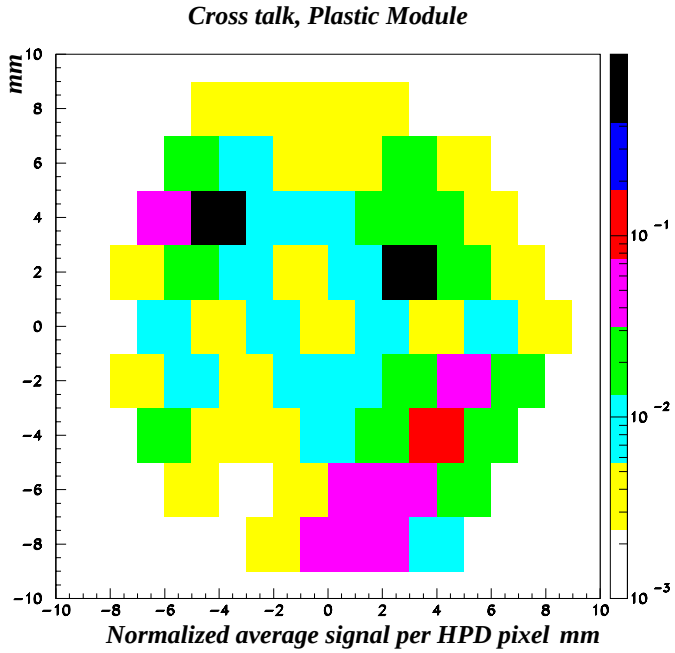


Figure 28: Display of the 61 HPD pixels. Selected events occur in pixels 13, 24 and 42. The signals are normalized to the maximum signal.

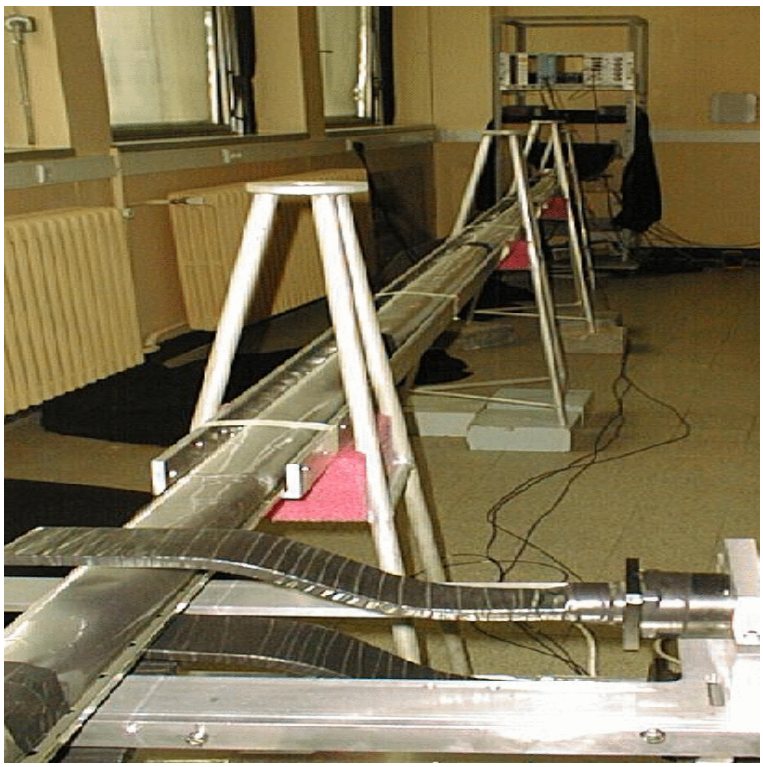

Figure 29: Picture of the liquid scintillator cosmics setup tested in Lyon with a HPD readout system

of cosmic ray data taking) the curve is fitted with a single exponential. The corresponding attenuation length, averaged on the 12 cells, is 5.8 m.

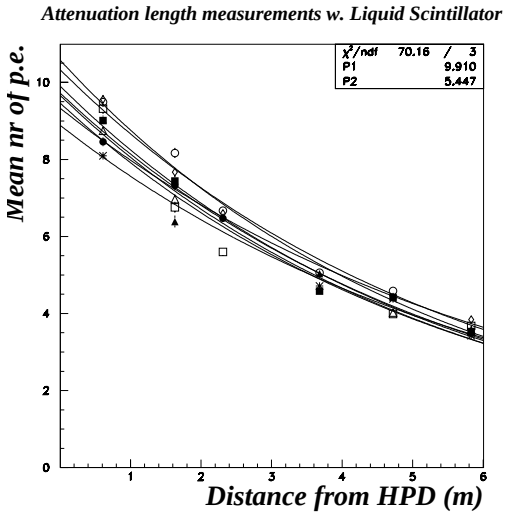


Figure 30: Variation of the light yield w.r.t. the distance to the HPD. The fitting curve is a single exponential.

### 5.2.2 Beam tests

The MIP response of the full scale liquid scintillator prototype was also investigated with the HPD readout system. In this experiment, a 6 m horizontal plane of 50 cells was read by one HPD on one side and one EBCCD on the other side. 2 horizontal and 3 vertical planes were also read by the EBCCD on one side. Lead bricks (5.6 cm of Pb) were sandwiched between the 3 plane "doublets" and variable amount of Pb was put in front of the first plane (the one connected to the HPD). Tests were performed at variable energies (2, 4, 6 and 8 GeV).

We present here the results for the MIP response. The spectra for one central cell is given in Fig. 31. The average number of photo-electrons 4.6 at 4m distance, is fully consistent with the one obtained with the cosmic ray setup at a comparable distance. The mip response and attenuation length are also consistent with a radioactive source measurement not shown here.

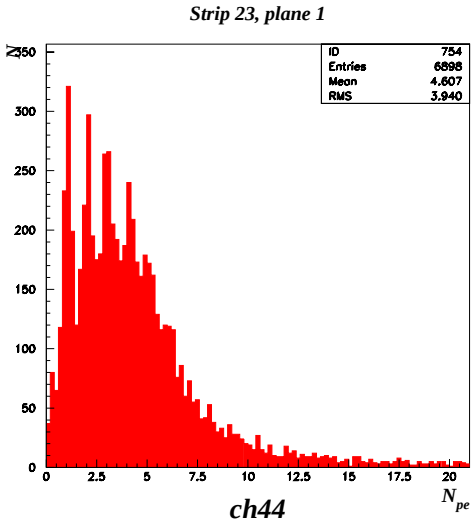


Figure 31: MIP response spectrum at 4 m from the HPD on a central cell (# 23). The average number of photo-electrons is 4.6.

# 6 Photodetector at the corners: an alternative design

The baseline option for the electronic detector in OPERA is a scintillator tracker with plastic scintillator strips, 6.7 m long, 1 cm thick and 2.6 cm wide, readout with WLS fibers and the Hamamatsu 64 pixels H7546 MaPMT placed at both ends of the fibers [12]. The geometry of the tracker is fixed by the choice of these elements. The basic units are sub-modules of 64 strips readout by two MaPMT's. Four sub-modules are assembled in situ to construct a whole scintillator wall. Two planes with strips orthogonal are coupled to form a $x-y$ tracker. Basic numbers for the baseline target tracker are recalled in Tab.3.

Table 3: Reminder of the number of elements in the baseline target tracker.

| # | per plane | 3 super-modules |
|---|---|---|
| strips | 256 | 36864 |
| units | 4 | 576 |
| MaPMT's | 8 | 1152 |

In this baseline design the photo-detectors are contained in the sub-modules with the front-end electronics. The main advantages of this solution, is the avoidance of optical connectors and the the modularity of the whole complex. Its main drawbacks as we see them are :

- low accessibility of the photo-detectors and the front-end electronics (in particular for the vertical strips planes);
- fragility of the modules (with photo-detectors and electronics embedded) during transportation and assembly;
- close coupling between the production of the scintillator modules and the photodetector and electronics assembly. We put both items on the critical path.
- large longitudinal dimensions of the sub-modules. The end-manifold length, around 40 cm, is imposed by the fibers bending radius, the photo-detector and cookie lengths, the electronic readout card and mechanical support. This extra length could interfere with the workings of the the brick manipulator robot. A reduction of this length could be welcome;
- large transverse dimensions imposed by the photo-detector. The end-manifold has a thickness of 32 mm : 30 mm due to the MaPMT thickness and 1 mm margin on each side. Probably larger margins will be needed. The increased length increases quadratically the scanning load for the events requiring a brick-to-brick track matching.

In this note we propose a possible alternative to the baseline option which foresees to locate the photo-detectors in the "corners" of the target tracker planes. The photo-detectors should be housed in metallic boxes attached to the transverse beams of the detector. This solution allows to overcome all the drawbacks stated before at the cost of the use of clear fibers and optical connectors (option retained by the MINOS collaboration, see Sec.6.3 for more details).

The transverse dimensions could be reduced down to the intrinsic width of the scintillator plus the mechanical support and tolerances (one can assume 22 to 25 mm transverse dimensions depending on the mechanical support). Furthermore the longitudinal end-manifold length is reduced to the minimum bending radius of the fibers (10 cm). The accessibility to the photo-detectors is better because there are no mechanical support (like springs...) in this corner part of the detector. Furthermore in the case we introduce a x-y plane coincidence the triggering signals are only traveling between four clusters of photodetectors/plane.

The transportation can be made separately for the passive elements (scintillator sub-modules) and the photo-detectors boxes. The scintillator and the photo-detector can be tested and calibrated first separately on the respective production sites and then connected together with the clear fibers for a global calibration test. This test could be performed either in the Gran Sasso or in one of the production sites.

This architecture is compatible with both plastic and liquid scintillator options. Furthermore it can be designed for a MaPMT or a HPD readout. We will present in this note a possible scheme with a new type of HPD designed by DEP and that will be available in Lyon in the coming months.

## 6.1 A possible candidate: HPD 163 pixels, "hot" S20

The main features of the HPD presented in this note (resolution, uniformity, linearity, low cross-talk and good quantum efficiency) have been evaluated in Lyon with the 61-pixels model available at that time.

Since then, DEP has developed for the BTeV collaboration an HPD with 163 pixels. The major change has been the re-design of the silicon chip. The R&D for this is now completed and the first tubes have been delivered to BTeV and another one could be delivered for OPERA in 3 month's time. The design of such a tube is displayed on Fig. 32. It will be a proximity focusing tube with a "hot" S20 photo-cathode.

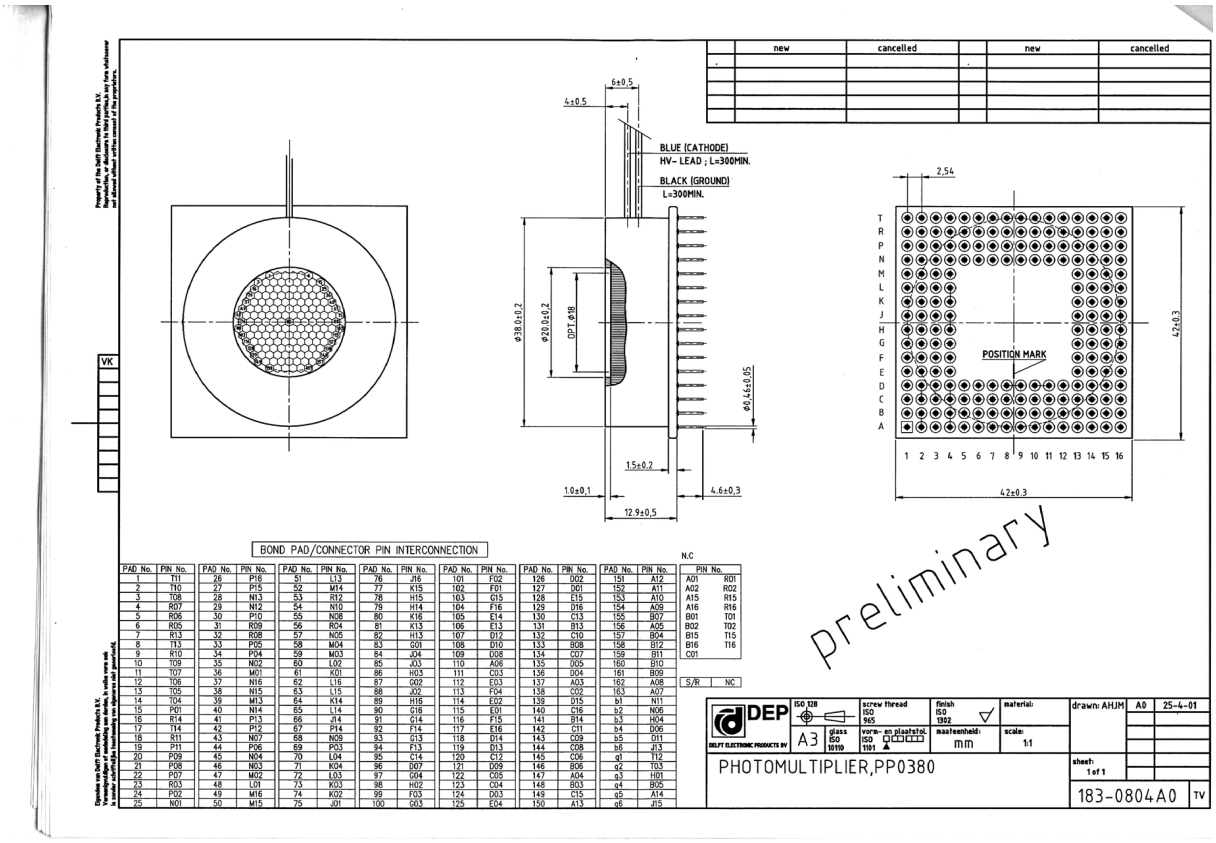


Figure 32: Preliminary design of the new 163 pixels, proximity focusing tube.

The tube is the same as the 61 pixels (same dimensions, see Fig.1). The PGA socket is larger (42 mm) and has 192 pins (17 of which are not connected). The pixels have still hexagonal shape with shorter dimensions (1.345 mm flat to flat instead of 2 mm), 1.57 mm$^2$ active area and 40 $\mu$m gap between adjacent pixels. Fig.33 gives the details of the PIN diode. The output capacitance is slightly reduced (3 pF instead of 4 pF).

The first estimations show that this imposes a maximal diameter of 1.1 mm for the fibers. The cross-talk of such a configuration needs also to be investigated.

## 6.2 Proposals for a tracker architecture

In the basic design 160 pixels of the HPD are connected to a scintillator sub-module. These 160 pixels correspond to 5 chips with 32 VATA (or the LAL chip) channels each. As mentioned before, the solution is compatible with either plastic or liquid scintillator. In the case of plastic scintillator, we could suppose that we stay close to the baseline design with only difference the location of the photodetectors and a slight reduction of transverse length. We could connect up to 320 strips on four HPD's for one plane (the fibers are readout at both ends). A total of 8 HPD's are necessary for a plane of $x - y$. The total

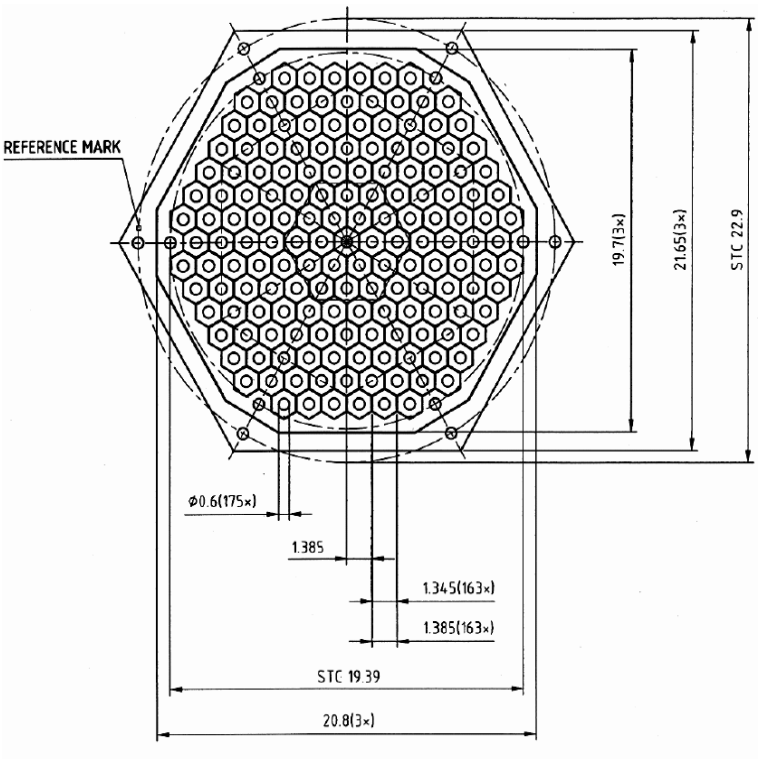


Figure 33: Design of the 163 pixels HPD PIN diode.

number of tubes for the OPERA detector is therefore 576 (that is half of the baseline proposal). The segmentation of the detector could be decreased by taking 2.1 cm wide scintillator strips.

In the case of liquid scintillator the segmentation could be easily varied. We will assume that the segmentation is $1 \times 1$ cm$^2$ (standard polycarbonate cells already tested by the collaboration). To keep the same number of readout channels, we propose to readout the fibers only at one end with a mirror (or some reflective material) deposited at the other end. Then we could gather 640 fibers on four HPD's for one plane. This requires 8 HPD's per $x - y$ plane just as in the previous case. Therefore 576 tubes are needed in this architecture also.

The increase in fiber length is balanced by the lower price of the liquid scintillator. In order to limit low sensitivity areas (far away from the photo-detector and therefore with the lowest number of photo-electrons due to the absorption along the fiber), the readout side may be alternated on each plane. We show 2 possible sketches for the module architecture on Fig.34. We see from these schemes that 2 HPD's are housed in one photo-detector box that is fixed in the corner. A light injection system using LED's can be housed in such boxes (the constraints in terms of weight and dimensions are released in the corners).

## 6.3 Optical connections

A critical point of the proposed architecture is the optical connection from the WLS fibers to the photo-detectors. The most efficient way to perform this connection is to use clear fibers which have a longer attenuation length than the WLS fibers. For instance the MINOS collaboration quotes an attenuation length of 14 m for the 1.2 mm Kuraray fibers. This connection gives the possibility to decouple the scintillator sub-modules (passive elements) from the readout (photo-detector and electronics). The drawback is the light loss in the connector. Nevertheless the MINOS collaboration have designed connectors with above 90 % absolute transmission.

For $\sim$ 90% absolute transmission, then the maximal light loss along a fiber starting from the center of the detector and going to a photo-detector cookie located in a corner (we assume 4 m length) is 30%. For the shorter clear fibers (with a maximal length assumed to be 1 m) the attenuation is 15%.

Two types of optical connections could be foreseen (Fig.35). The first one (type (a)) (MINOS like) starts from the assembly of WLS fibers with a small gap between fibers and then a symmetric connection

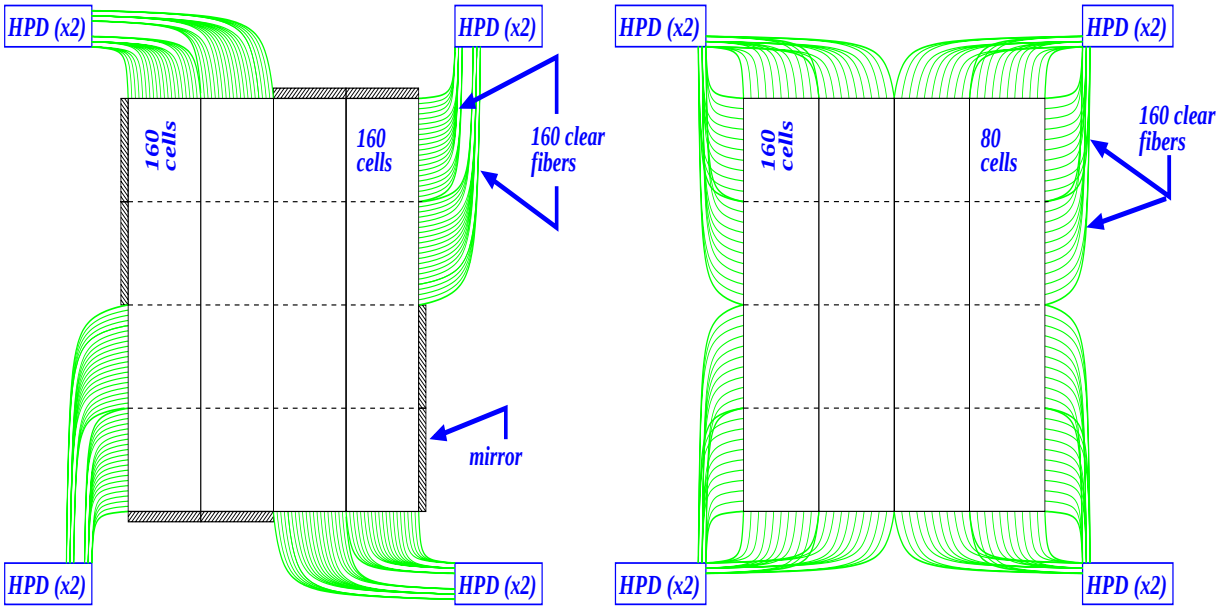


Figure 34: Possible sketches for the tracker architecture with one or two ends readout (resp. left and right plot). The figure shows the $x$ and $y$ cells. The clear fibers are also drawn (green lines). They are connected on the HPD boxes which house 2 HPD's 160 pixels to fix the segmentation. In the left plot, The hatched areas represent the mirrors at the end of the fibers.

with clear fibers. This offers the advantage to have short connectors (with a good relative alignment) that should be easier to produce. In the second procedure (type (b)) we use long bars in which the fibers are glued. The WLS fibers are cut at the exact dimension of the sub-modules, without extra length. As the absorption in these fibers varies rapidly at short distances, we avoid large spreads in the light yield. The total extra length of the fibers out of the sub-modules is also reduced w.r.t. the first procedure. The weak point of this procedure is the absolute transmission that could be achieved with such a connector. Studies are underway in Lyon on a liquid scintillator prototype realized in collaboration with CERN (see Sec.6.4).

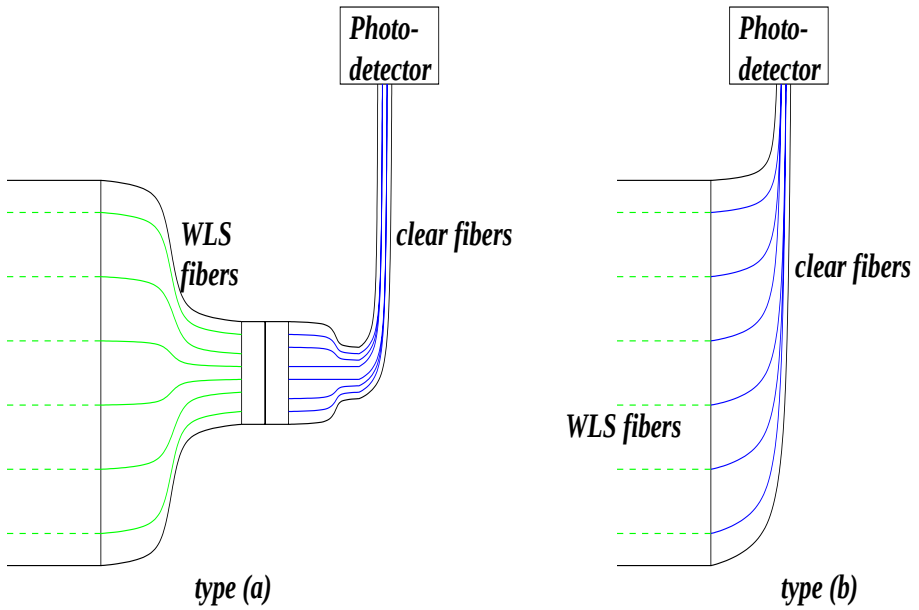


Figure 35: Sketch for two possible optical connections between WLS and clear fibers.

## 6.4 Liquid scintillator prototype

The purpose of this prototype is the study of the light yield with the standard liquid scintillator used by the collaboration, the standard $1 \times 1$ cm$^2$ polycarbonate cells loaded with $TiO_2$ and clear fiber connection of the second type (so-called type (b) in the previous Section). A general view of the prototype is shown in Fig.36. It consists of 60 cells closed at each ends by a $\sim 3$ cm silicon glue end-cap and the first half of an optical connector. Each cell is cut at its end over $\sim 1$ cm in order to allow the liquid to go from cell to cell during the filling procedure (see detail on Fig.36).

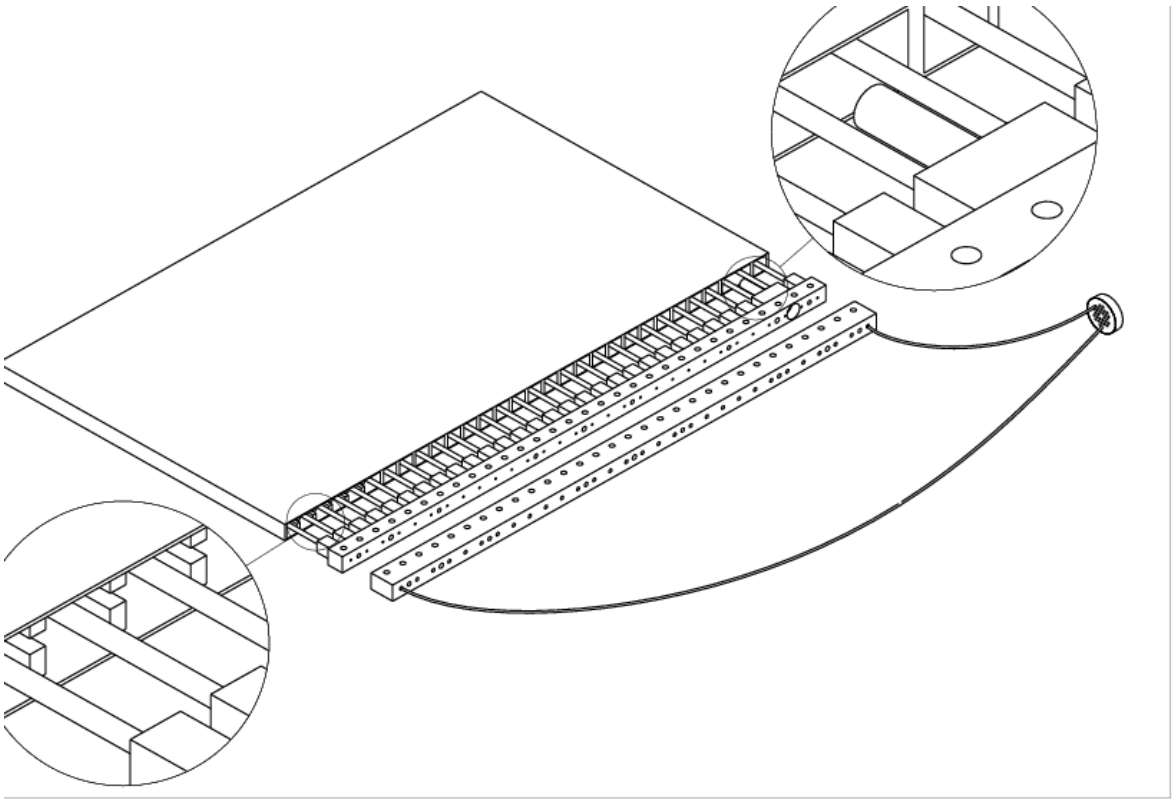

Figure 36: Design of the liquid scintillator prototype.

The first half of the optical connector is made of two $\sim 33$ cm plastic bars (PVC will be used for the prototype) that are detailed in Fig.37. Each bar has 30 holes for the fibers (we will use 1.2 mm WLS and clear fibers), 30 holes on the top for the fiber gluing, 6 alignment pins and 6 screws. One 5 mm diameter hole is pierced into the bar for filling. A 5 cm tube goes from this hole inside the detector (outside of the silicon glue end-cap). An external tube is used to connect to the filling pump. Once the filling has been completed this external tube is removed and replaced with a dedicated screw for liquid tightness. The second half of the connector is symmetric, except for the filling hole that is not necessary.

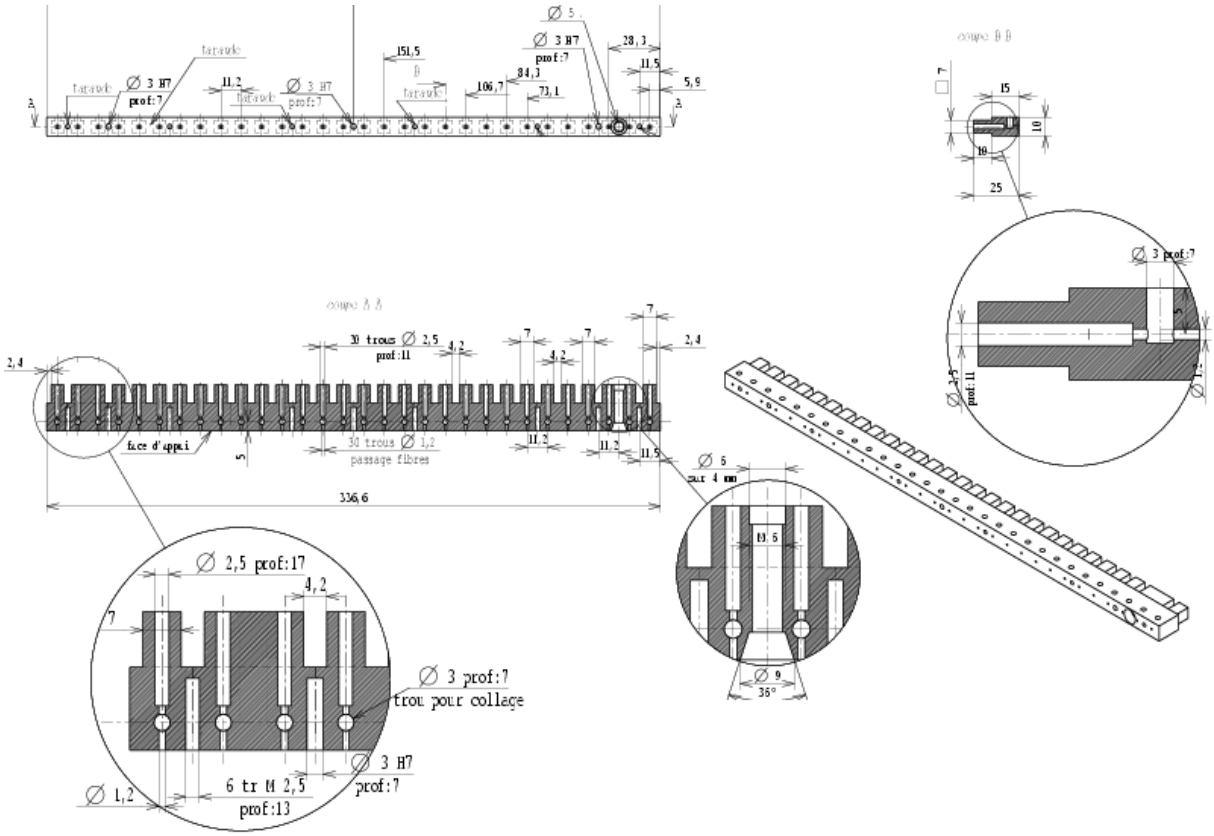


Figure 37: First half of the optical connector (WLS fiber side).

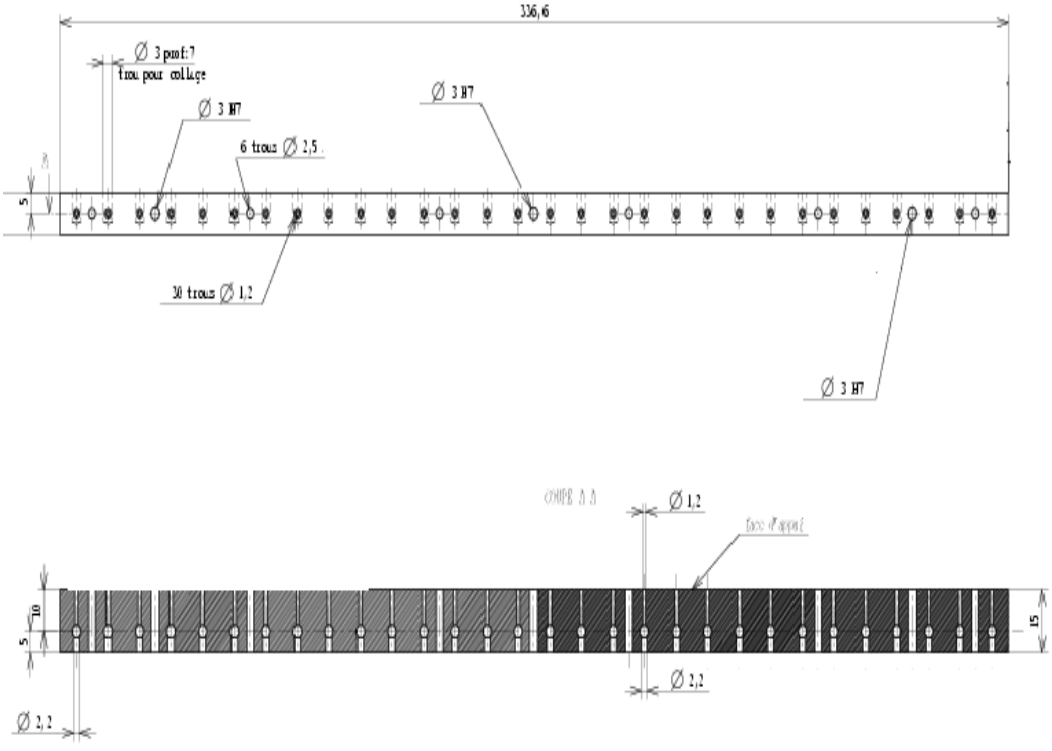


Figure 38: Second half of the optical connector (clear fiber side).

# 7 Trigger

The upcoming milestone does not concern the trigger and the data acquisition. Nevertheless the choice of a tracking device and detector imposes constraints due to singles rates, data loads, dead-times and spurious extraction of bricks.

Furthermore, a large part of the Lyon group test beam activity concerned the validation of a full data acquisition and readout chain from the photodetector to the workstation. We analyze the possibilities offered by such a scheme for triggering and readout. The scheme does not depend on the photodetector (MaPMT or HPD) option and it can implement either full autotriggerability or a x-y coincidence trigger. If one applies some modifications to the front end this scheme is also applicable to RPC's.

## 7.1 Dead time

In the previous sections, we presented the VATAcg front-end scheme.

We briefly recall its principle: it consists of 64-channel chips where the charge is preamplified and then shaped through a fast and a slow shaper. The slow shaper (VA) has a rise-time of 1-2 microseconds and the fast shaper (TAcg) has a rise-time of $\sim 70$ nanoseconds. The signals of the fast shaper pass through a discriminator, and their OR serves as a hold signal to sample on the peak the charge accumulated over the 64 channels of the VA part. The same signal initiates the readout sequence which clocks the 64fold multiplexed data into an ADC. One thus has a fully trigerless scheme (scheme A). The current readout speed determined by the multiplexer (5 MHz) does not permit the dead-timeless readout of a 160 pixel HPD by only one ADC[3].

The dead-times of scheme A is given by the formula:

$$\text{Dead time} = (1 - e^{-D}) \qquad D = N \times r \times (t_p + N * t_r)$$

where N is the number of channels (e.g 64) and $r$ is the singles rate per channel.We assume a shaping time of $t_p = 2$ microseconds and a 5 MHz readout clock ($t_r = 200ns$/channel). For $D \ll 1$ we have of course $(1 - e^{-D}) \to D$. Figure 39 shows the percent of dead time as a function of the singles rate of one channel for a 64fold readout and 3 clock speeds. A nominal 5% dead time is reached for a singles rate of 50 Hz and 5 MHz clock readout. By doubling the readout speed one obtains the same limit for 100 Hz, and at 20 MHz one obtains 150 Hz. For comparison the same limit for an option where 160 pixels are multiplexed in one ADC, and 20 MHz readout is 30 Hz. In conclusion, with the present and forseable readout speeds the full autotriggerability without dead time can be achieved only if we keep the 64 granularity for the readout chain.

Alternatively one can use a x-y coincidence. We call this scheme B. The current prototype readout card ORCA accepts external triggers and thus permits the formation of a global bi-plane (XY) coincidence using the fast TA OR logical signals of the 16 to 20 front-ends. The longest length along the perimeter of one plane is $\sim$ 14m adding a maximum round-trip delay of 100 ns, well below the 2 microseconds available. In this scheme the TA signal of an x front-end issues a hold, only after validation from a coincidence in time with the corresponding y-plane. The same happens for the y-plane. This scheme has the advantage that it keeps the proper timing between the TA and the peak time of the VA, that only the front-ends with a signal are readout, and that it exhibits as is shown below robustness to high rates. The disadvantage of this scheme is the need for two extra cables coming out and in from the card, and the need for an extra coincidence forming module.

We calculate the rate of coincidences for this scheme by using the formula:

$$r_c = 2 \times N^2 \times r^2 \times G$$

where $N$ is the number of strips in a plane and $G$ is the coincidence gate. For the 2.6cm strip width option we have 512 channels/plane while for the 1cm option we have 640 channels/plane. A 100 ns gate G can largely accommodate delays and different decay times.

Figure 39 shows the percent of dead-time for a 160fold readout, 1cm width strips read on one side (640 channels/plane) as a function of singles rate. We have the nominal 5% dead time for singles rates of 150, 200 and 250 Hz with 5, 10 and 20 MHz readout clock frequency respectively. The 160fold readout (1 ADC for 160 channels) becomes robust to fluctuations in singles rates.

[3]Note that in the case of the 160 channel HPD, we would need five 32channel VATACG chips that could either be readout by a single ADC, or have 2 HPD's read by 3 separate autotriggerable 64 ADC chains; keeping the 64fold electronics granularity.

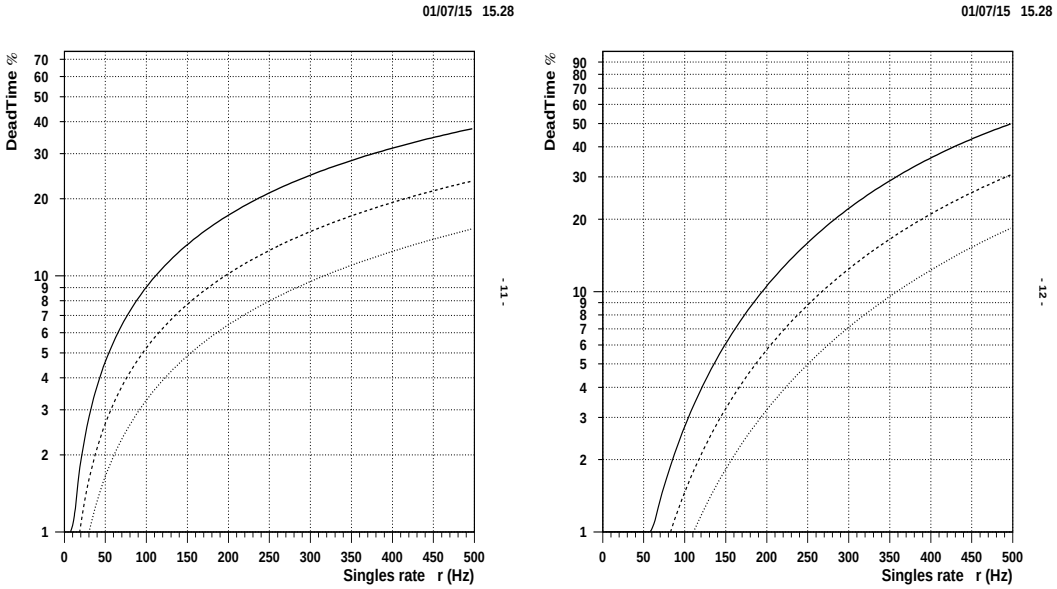


Figure 39: Left: % of Dead time as a function of a single channel rate, in the case of a 64fold multiplexing A) Solid line: 5 MHz clock B) Dashed line: 10 MHz clock C) Dotted line: 20 MHz clock Right: % of Dead time as a function of a single channel rate, in the case of a x-y coincidence in a 640 channel plane A) Solid line: 5 MHz clock B) Dashed line: 10 MHz clock C) Dotted line: 20 MHz clock

## 7.2 False extractions

Another question by the referees is the possibility of a random coincidence simulating an event trigger within the spill time. We first applied 2 kinds of trigger for the most sensitive events: $\tau \to e$ and $\tau \to \pi$ quasielastic (QE) events. The first trigger demands the coincidence of at least 2 consecutive planes (4 planes in all if one counts X and Y planes), and the second demands a single plane x-y coincidence but asks for a large number of pe's (10) and at least 3 strips hit. The effect of the OR of these 2 triggers on the QE events mentioned above can be seen at table 4. The Plastic and Liquid scintillator options are taken with 6 and 9 p.e's at the center respectively. The table intends to show that the above trigger criteria have a good trigger efficiency.

| Condition | Liq $\tau \to e$ | Liq $\tau \to \pi$ | Plast $\tau \to e$ | Plast $\tau \to \pi$ |
|---|---|---|---|---|
| 1 plane coincidence | 0.99 | 0.995 | 0.99 | 0.995 |
| 2 planes coincidence | 0.75 | 0.93 | 0.73 | 0.93 |
| 2 planes OR electron | 0.92 | 0.975 | 0.905 | 0.97 |

Table 4: Trigger efficiency for different scintillator options and the most sensitive QE events. For the details of the triggers see the text.

Now the next question is whether these very loose criteria, will induce an unacceptable rate of false extractions. The nominal tolerable level has been set to 0.3 bricks/day. We did not evaluate the electron trigger random rate since it demands a more detailed knowledge of the p.e. spectrum (including radioactivity) that we do not currently have. The cut of 10 p.e is sufficiently high to ensure that we will not have any surprises.

Coming to the 2 XY plane coincidence trigger, on can use the following formula to estimate the rates:

$$N_{extr/day} = 72 \times N^2 \times [2 \times (2 \times 3 \times r^2 G)^2 G] \times t_{livetime/day}$$

where the term $(2 \times 3 \times r^2 \times G)$ calculates the random doublet coincidence of a x strip with 3 adjacent x strips of the next wall, the y-doublets will have of course the same rate. The term within brackets calculates the coincidence of a x-doublet with a y-doublet in a fourfold coincidence. The overall rate

has to be multiplied with the number of strip combinations/plane $N^2$ (N=256 or 640), the number of consecutive planes (72) the total live-time with beam on per day (220 milliseconds).

One can see in figure 40 that up to extreme values of singles rate the acceptable limit for false brick extractions per day is satisfied.

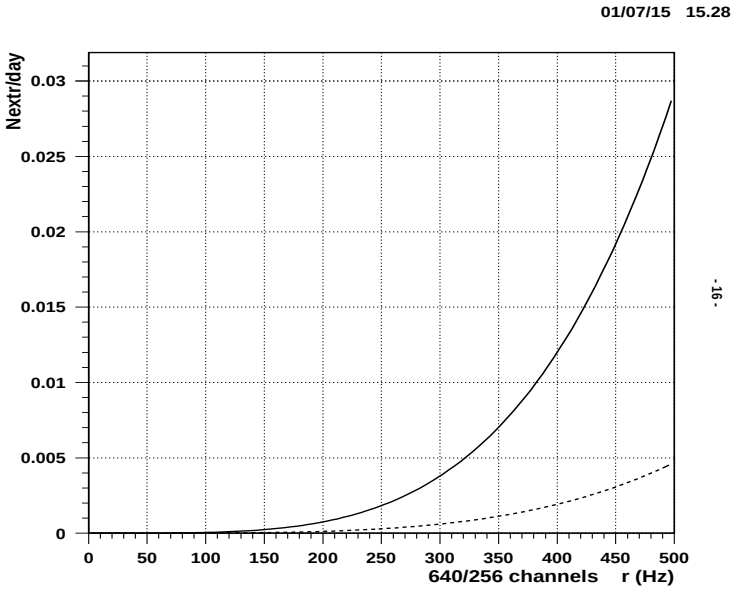


Figure 40: Number of events per day that satisfy the criterium of a double x-y plane coincidence as a function of singles rate per channel. Solid line a 640 strip plane, Dashed a 256 strip one.

In conclusion a 100 Hz rate is acceptable for fully autotriggerable rates (scheme A) and 64fold readout, while plane coincidences (scheme B) can raise the tolerance to 150-200 Hz. These rates are largely consistent with the nominal limits for false extractions (0.3 bricks /day).

# 8 Data acquisition

The next question one has to answer is whether the above rates, can give reasonable data bandwidths. In the current implementation we use a largely redundant load of 12 bytes/hit (12 bit ADC plus label plus time stamp plus many and debug control bits). If one therefore assumes a singles rate of 100 Hz per channel, one obtains a data rate of 0.61 Mbits/s per group of 64 channels.

More generally figure 41 shows the data bandwidth in MBits/s as a function of singles rates, for the autotriggerable scheme (A) with 64 channels per ADC and 2 readout times (5 and 10 MHz) and the same bandwidth for scheme B and a 640 channel plane. Below 150 MHz where one has quasi dead-time less operation, the bandwidth never exceeds 1 Mbit/s.

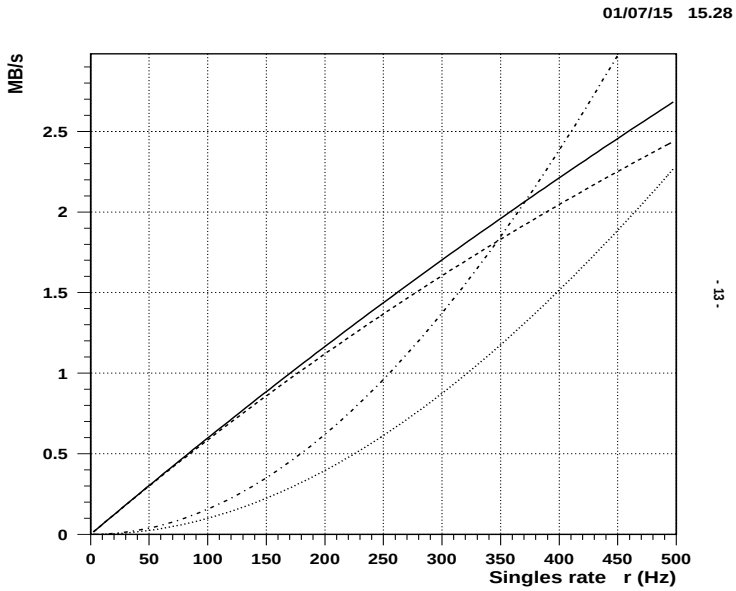


Figure 41: Data bandwidth in MBit/s as a function of the singles rate per channel. Solid line Autotriggerable scheme A and 10 MHz readout clock. Dashed line same as above with 5 MHz clock. Dotted line and dashed-dotted line: triggering scheme B, with x-y plane coincidence and 5 and 10 MHz readout clocks respectively

The data rate estimated above is a low rate for high energy physics standards, and allows the use of an Ethernet capable device like ORCA close to the sensor. The basic idea of our scheme is therefore to build a distributed acquisition system on Ethernet, made of a few hundred nodes, each node corresponding to one or at most two front-end modules. Each node will be controlled and readout by an embedded Ethernet chip and will be therefore transparently visible on the network. Each module is autonomous and possesses its own Internet Protocol (IP) address and has all the necessary functions for slow control, monitoring, and readout of the front-end analog chip through simple web browser tools.

The number of nodes (64 channels/node) one supermodule with readout at both sides and 256 strips/plane is 384. In the case of the 1cm version and 640 strips per plane with one-sided readout, one has 480 nodes. In both cases one might also consider the possibility to group the channels to 128 channels/node, having 192(240) nodes in total. We use below the 192 nodes model to evaluate the overall performances of the data-acquisition. The event trigger rate is dominated by the photo-detector dark current and possibly radioactivity. The peak rate does not change substantially this estimation.

The overall acquisition scheme, as we propose it, is shown in figure 42 The global architecture is based on two levels. The first level contains 192 nodes directly connected to 4 concentrating switches. Each switch has 48 10/100 Mbit input links and 2 Gigabit Ethernet outputs (we currently evaluate the BATM Titan T5 model [14]). The 4 Gigabit outputs go to a $4 \times 4$ Gigabit switch (Equally Titan T5) and can be distributed to up to 4 workstations (second level). The system can be easily upgraded and scaled up if more processing power is needed.

K. Korcyl of the ATLAS second level trigger group, has kindly agreed to simulate the architecture

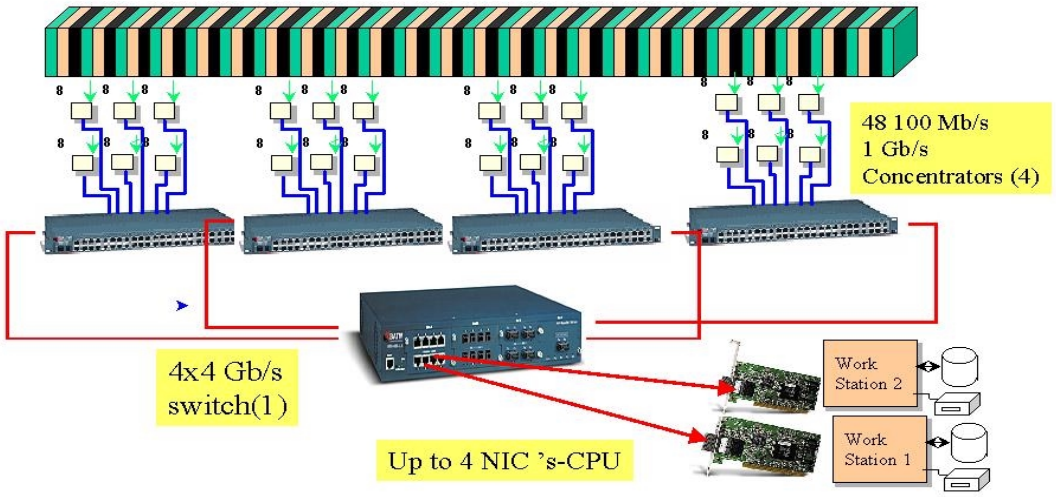


Figure 42: A DACQ scheme for 1 supermodule

proposed for OPERA with the finite state machine simulator Ptolemy. He has simulated the traffic of one million Ethernet packets, with the architecture as is presented in the figure 42. The true parameters of the commercial switches and concentrators by BATM [14] have been incorporated in the simulation.

Figure 43 shows the probability that an Ethernet packet (1460 bytes) has to to wait above a certain time given in the abscissa before it is delivered. It is an index of congestion. One sees therefore that for bandwidths below 5 Mb/s/channel and 2 workstations, the probability that the packets will NOT be delivered to their destination after 300 microseconds is 1 in a million. This latency gives a really comfortable margin for sorting, software triggers and other possible decisions. In the same figure one can also see that for a 10 Mbits/s/channel bandwidth, and 2 workstations, we reach at the limits of the total aggregate bandwidth and the latency times flat and will produce congestion.

Figure 44 on the other hand shows the probability that one packet finds already another packet serviced in the input queue of the switch, and has therefore to wait. One again sees that up to 3 MBit/s/channel, the packets find with a close to 100% probability the queue empty and they are sent to their destination without delay. The TCP/IP protocol is not yet simulated, but it will be implemented before the end of the summer. One would then also be able to predict the CPU load due to the handling of the traffic, and therefore the time of available CPU for event building.

The advantages of this Ethernet solution are:

- Stability: since one uses a widely distributed industrial standard, with an expansion future of at least 10 years in front of it. Low power, low cost ($\sim 10 - 15\$$) processors become continuously available for new applications as mobile phones, intelligent domotics etc. High speed products such as Gigabits switches are available at low cost and 10 Gigabits products are now emerging.

- Synergy: All LHC experiments plan to make their high level trigger level decisions involving Terabytes of data through Ethernet and concentrating switches. In fact we have already used ATLAS 2nd level trigger expertise (simulations by K. Korcyl).

- Transparency and simplicity of the software which guarantees easy maintenance. The final processor we intend to use operates under Linux and the code can be written directly in C by any physicist.

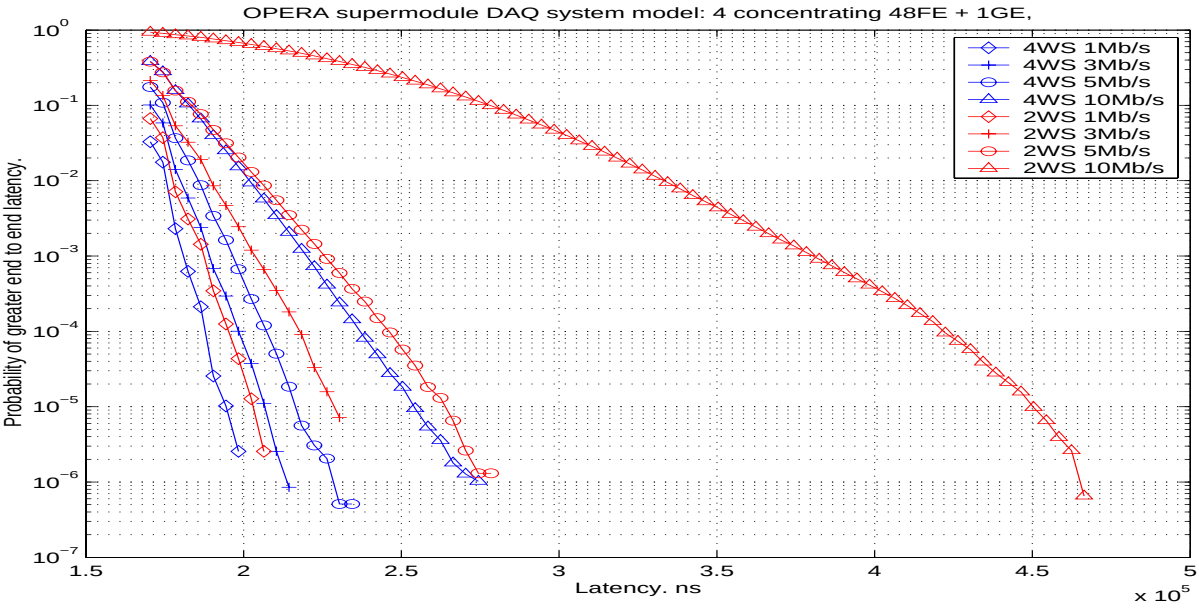


Figure 43: Probability of maximum latency vs latency

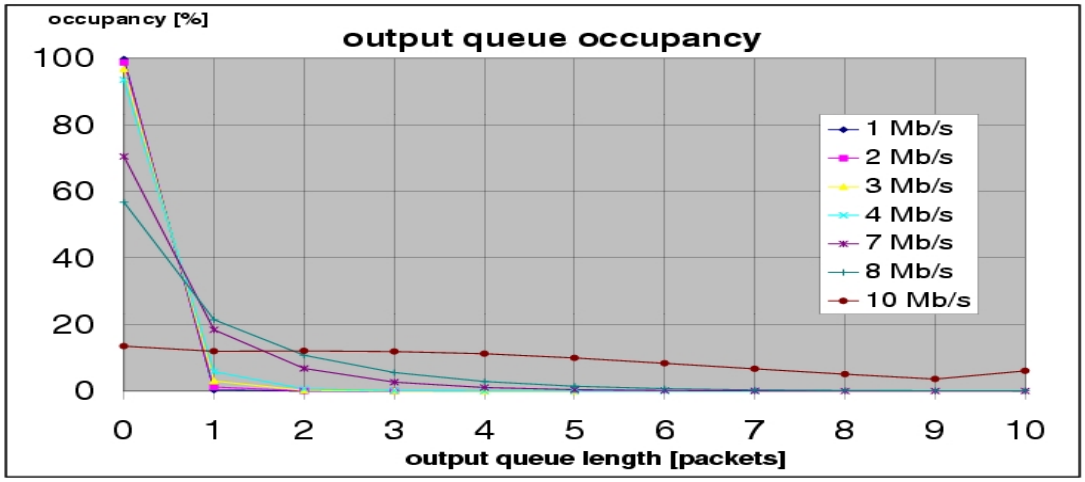


Figure 44: Probability of finding a queue full

# 9 Conclusions

We can recapitulate our findings as follows:

- We have evaluated the HPD as a possible photodetector for OPERA. Its excellent resolution (S/B=6), uniformity (2%) and low cross talk (2%) make it a very good candidate for the target tracker scintillator readout. Two of its possible limitations: the high dark current (1kHz/pixel) and the high cost, are alleviated by the fact that DEP has produced new HPD's that have a high pixelisation number (161) bringing down the cost to 22 Euros/channel, and have a photocathode (hot S20) which has a dark current rate of the order of 60 Hz.

- We have evaluated the commercial front-end chips VATA. They satisfy most of our specifications. They have excellent uniformity, good linearity and exhibit autotriggerability down to the single photoelectron. The noise and uniformity obtained are good, though a factor 2 reduction in noise is possible trhrough a redesign of the PCB. This reduction would help a lot for a fully efficient single photoelectron trigger. The multiplexer readout speed should be also increased to 10-20 MHz in order to have dead-timeless operation, in the case of the HPD readout.

- We have constructed a prototype intelligent readout card (ORCA) digitizing the front-end with a 12bit ADC, sequenced by a FPGA and controlled by an Ethernet controller. Embedded slow control, monitoring and readout functions are directly accessible from the network by TCP/IP or a simple WEB browser. The system has been validated in beam tests. We obtained 1 Mbit/s data throughput/card, and we hope to increase this bandwidth to a good fraction of 100 Mbit/s, using a new ethernet controller.

- We have constructed a small plastic scintillator prototype, which we have exposed to the beam at CERN, and intend to take it to Gran Sasso for the measurement of the response to ambient radioactivity.

- We used the full acquisition chain (HPD-VATA-Ethernet DACQ) to measure the MIP response and attenuation lengths of both the liquid and plastic scintillator options. While the numbers could be improved (8.6 close to the photodetector for the plastic and 4.5 at 4m for the liquid scintillator), the current photon budget remains acceptable. It is also interesting to note, that for the plastic scintillator we find the same numbers as Strasbourg, despite the fact that we use an extra connector, proving that the trasmission of the optical connector is very good.

- We have also constructed a long series of cookies and connectors and evaluated their transmission with good results (transmission efficiency above 80% for the connectors). A connector technology with transmissions above 90% is not beyond reach, according to the experience of MINOS and ours.

- We propose for reasons of compatibility with the brick handling robot, ease of access, geometry of the brick planes, decoupling of the scintillator construction from the photodetector choice and versatility for the type of photodetector to be used an alternative geometry where the photodetectors are put in the corners. We present a prototype design of the optical connectors needed for this architecture

- Up to 100 Hz of singles rate per strip, give acceptable dead-times and false extractions of bricks/day. The use of an x-y coincidence per plane, while it perturbs the module autonomy, gives larger margins of accepted singles rates by a factor almost 2.

- We finally present the progress of our work concerning the simulation and design of a fully ethernet readout scheme, using the above readout cards.

# References


[1] G. Moret OPERA note

[2] Site DEP, http://www.dep.nl/index.htm

[3] "Ultra bright LED light injection calibration system for MINOS", B.Anderson, A.Anjomshoaa, P.Dervan, J.A.Lauber, J.Thomas, NIMA 423(1999)320-327.

[4] Matsusada Precision Inc., 745 Aoji-cho Kusatsu Shiga 525-0041, Japan.

[5] J.Seguinot, private communication.

[6] O. Toker et al. NIM A340(1994)572 et NIM A301(1991)506

[7] Site IDE-AS, http://www.ideas.no/index.html

[8] "Ethernet network-based DAQ and smart sensors for the OPERA long-baseline neutrino experiment", C.Girerd, S.Gardien, J.Burch, S.Katsanevas, J.Marteau

[9] http ://www.agilent.com

[10] Standard for a Smart Transducer interface for sensor and actuators - Transducer to Microprocessors communication protocol and transducer electronic data sheet (TEDS) format. 1997- ISBN 1-5593-7963-4.

[11] Plastic Scintillator Target proposal R. Arnold et al. IreS/OPERA note

[12] OPERA proposal "An appearance experiment to search for $\nu_\mu \longrightarrow \nu_\tau$ oscillations in the CNGS", CERN/SPSC 2000-028, SPSC/P318, LNGS P25/2000, July 10, 2000

[13] http://www.axisdeveloppers.com

[14] http://www.batm.com